Lithos 150 (2012) 209–226

Contents lists available at SciVerse ScienceDirect

Lithos

journal homepage: www.elsevier.com/locate/lithos

Origin of the granulite enclaves in Indo-Sinian peraluminous granites, South China and its implication for crustal anatexis

Liang Zhao [a,b], Feng Guo [a,*], Weiming Fan [a], Chaowen Li [a], Xiaofeng Qin [c], Hongxia Li [a]

[a] State Key Laboratory of Isotope Geochemistry, Guangzhou Institute of Geochemistry, Chinese Academy of Sciences, Guangzhou 510640, China
[b] Key Laboratory of Marginal Sea Geology, South China Sea Institute Oceanology, Chinese Academy of Sciences, Guangzhou 510301, China
[c] Institute of Mineral Resources Chinese Academy of Geological Sciences, Beijing 100037, China

ARTICLE INFO

Article history:
Received 30 June 2011
Accepted 23 February 2012
Available online 3 March 2012

Keywords:
Crustal anatexis
P–T path
Restite
Granulite enclaves
Indo-Sinian peraluminous granites
South China

ABSTRACT

Metasedimentary granulite enclaves hosted in the Indo-Sinian Darongshan–Shiwandashan granite belt from the southeastern Guangxi province, South China, experienced a three-stage metamorphic evolution: (1) the early prograde metamorphism in the stability field of sillimanite at ~800 °C; (2) the peak metamorphism with a mineral assemblage of spinel + quartz at 7.5–8.0 kbar and 950–1000 °C (260–250 Ma); and (3) a near-isothermal decompression stage with orthopyroxene + plagioclase and orthopyroxene + cordierite symplectic textures at 3.2–3.7 kbar and 790–820 °C (240–230 Ma). The clockwise *P–T–t* path suggested that the granulite enclaves have undergone initial crustal thickening and subsequent rapid exhumation and cooling history.

The granulite enclaves show peraluminous affinities (A/CNK = 1.11–3.14, A/CNK = $Al_2O_3/(CaO + Na_2O + K_2O)$ in molecular ratio) with Al_2O_3 up to 25.31%; chondrite-normalized REE patterns similar to those of upper continental crust; relative Rb, Ba, Th, LREE, K, Zr and Hf enrichment and Sr, Nb, Ta, P and Ti depletion in primitive mantle-normalized spidergrams; and highly radiogenic Sr ($^{87}Sr/^{86}Sr(i) = 0.71295–0.74273$) and nonradiogenic Nd ($\varepsilon_{Nd}(t) = -14.8$ to -11.2). Systematic elemental variation trends from the granulite enclaves to the host granites, and similar Sr–Nd isotope compositions in the enclaves and the host granites, indicate that the two have a coherent origin — the granulites were restites of the host granites. The granulite enclaves can also be subdivided into two groups: high-$^{87}Sr/^{86}Sr(i)$ (>0.7303) and low-$^{87}Sr/^{86}Sr(i)$ groups (<0.7135). The estimated magma source for the host granites may contain 10–40% low-$^{87}Sr/^{86}Sr(i)$ and 60–90% high-$^{87}Sr/^{86}Sr(i)$ granulites.

P–T–t path and geochemical features of the granulite enclaves, temperature estimation for the host granites, and previous geochronological data, indicate limited dehydration melting of the metasedimentary protoliths during the prograde and peak metamorphic stages. Instead, large scale crustal melting may have occurred during the stage of exhumation and uplifting of the lower-middle crust.

1. Introduction

The Yangtze and Cathaysian blocks, two important Precambrian microcontinents, were believed to have amalgamated and collided along the Neoproterozoic along the Jiangnan Orogen, to form the South China block (SCB) (Li et al., 2002a, 2002b, 2006, 2008, 2009; Ye et al., 2007). Nevertheless, paleogeographical reconstruction in the southern and middle segments of the suturing belt indicated that a Paleozoic SW-trending remnant marine trough existed between the two blocks. This was termed as the Qin-Fang Trough (BGMRGX, 1985; Li et al., 1994; Liang and Li, 2005; Liang et al., 2004; Qiu and Liang, 2006; Xu et al., 2001a; Yin et al., 1999). Following the closure of the Paleo-Tethys along the Song-Ma suture and the subsequent collision between the SCB and the Indochina block (Lepvrier et al., 2008; Trung et al., 2006), this marine trough was ultimately closed by the end of Permian (BGMRGX, 1985; Li et al., 1994; Liang and Li, 2005; Liang et al., 2004; Qiu and Liang, 2006; Xu et al., 2001a). During the Indo-Sinian orogeny, both the Indochina block and the SCB experienced unusual high-grade metamorphism. For example, the Indochina block experienced ultrahigh-temperature (UHT) metamorphism recorded from the Kontum massif (Nakano et al., 2004, 2007, 2009; Nam et al., 2001; Osanai et al., 2001, 2004; Owada et al., 2006, 2007), and the Shiwandashan–Darongshan and Yunkaidashan areas in the SCB experienced high-temperature (HT) granulite-facies metamorphism (Chen et al., 2011; Peng, 2006; Wang et al., 2007; Zhao et al., 2010, 2011). The heat supply for these high-grade metamorphic events is still unclear. However, several studies have considered a possible genetic link between this metamorphism and the impact of Emeishan plume activity at ~260 Ma (Chen et al., 2011; Owada, et al., 2007; Peng, 2006, Zhao et al., 2010, 2011).

The Darongshan–Shiwandashan granite belt (DSGB) is located at the southwestern end of the joint between the Yangtze and the Cathaysian Blocks. It is well known as one of the largest Mesozoic peraluminous (or S-type) granitoid complexes in South China (BGMRGX,

* Corresponding author. Tel.: +86 20 85290280; fax: +86 20 85290130.
E-mail address: guofengt@263.net (F. Guo).

0024-4937/$ – see front matter © 2012 Published by Elsevier B.V.
doi:10.1016/j.lithos.2012.02.015

1985). Because of its special tectonic locality, this granite belt has been considered to be a particularly useful location for probing into the Indo-Sinian orogeny related to the collision between the Indochina block and SCB (Chen et al., 2011).

Enclaves are often found in peraluminous granites. These enclaves can provide information about the source rocks, unexposed middle and lower crustal rocks, and petrogenetic processes not readily available from the host granites (Anderson et al., 1998; Chappell et al., 1987; Didier and Barbarin, 1991; Waight et al., 2001; White and Chappell, 1977). Metasedimentary granulite enclaves are abundant in the Indo-Sinian peraluminous granites from the DSGB. In recent years, many papers have been published discussing the origin of these granites (e.g., Charoy and Barbey, 2008; Chen et al., 1995, 2011; Deng, 2003; Deng et al., 2004; Fang, 1989; Hsieh et al., 2008; Peng et al., 2004; Qi et al., 2007; Zhao et al., 2010, 2011), and their hosting granulite enclaves (e.g., Du et al., 1999; Pang, 2001; Peng, 2006; Peng et al., 2004; Wang, 1987; Zhao et al., 2010, 2011). Two possible tectonic settings of the granitic magmatism have been proposed: (1) anatexic products formed during continental collision (e.g., Chen et al., 1995, 2011; Deng, 2003; Deng et al., 2004; Fang, 1989; Hsieh et al., 2008; Qi et al., 2007); and (2) crustal melts of post-collisional extension (e.g., Charoy and Barbey, 2008; Peng et al., 2004; Zhao et al., 2010, 2011). Debate also continues about the origin of the granulite enclaves. Wang (1987) first reported the existence of the enclaves in the area, and considered them to be derived from the crust, existing as unmelted relicts of the deep-melting granites. Du et al. (1999) and Pang (2001) estimated the temperature and pressure of the granulite enclaves. The two studies suggested that the granulite enclaves were derived from middle to lower crust and were formed by dynamothermal regional metamorphism. Peng (2006) reported that the peak metamorphic temperature for the granulite enclaves exceeded 1000 °C. Based on zircon and monazite U–Pb ages, Peng (2006), Zhao et al. (2010) and Chen et al. (2011) proposed that the origin of the granulite enclaves was genetically related to the Emeishan plume activity. Yet, debate continues about the *P–T* conditions of the granulite-facies metamorphism, the relationship between the granulite enclaves and the host granites and the causes for the extensive crustal anatexis.

In this paper, we present a comprehensive study on the granulite enclaves hosted in the Indo-Sinian peraluminous granites from the DSGB, including metamorphic texture, mineral compositions, whole-rock geochemical and Sr–Nd isotopic data. The purposes of this study are: (1) to reconstruct the metamorphic conditions and *P–T* path; (2) to understand the origin of the granulite enclaves and their relationship with the host granites; and (3) to discuss the possible mechanism of the granulite-facies metamorphism and crustal anatexis.

2. Geological background and petrography

The DSGB, covering an area of ~10,000 km^2, lies in the southeastern Guangxi province, South China (Fig. 1a). It is bordered by the Yunkaidashan Mountain (YKM) to the east and the Shiwandashan Basin to the west, with the NE-trending Bobai–Cenxi and Lingshan–Tengxian faults as its boundaries, respectively (Fig. 1b). It was ever a part of the Qin-Fang Trough in the Paleozoic, and during this period voluminous sediments with a thickness of 21–25 km were deposited (BGMRGX, 1985). The closure of the Qin-Fang Trough occurred by the end of Permian, and this triggered regional deformation and metamorphism (Chen et al., 2011; Wang et al., 2007; Zhao et al., 2010, 2011). Subsequent melting of the metasedimentary protoliths formed the widespread peraluminous granites at 240–230 Ma (Chen et al., 2011; Deng, 2003; Deng et al., 2004; Zhao et al., 2011).

From north to south, the DSGB consists of Darongshan, Pubei, Taima and Jiuzhou plutons (Fig. 1), intruding Paleozoic low-grade metasedimentary rocks like slates, sandshales, siliceous and carbonate rocks. The Darongshan pluton is located in the northeastern part of the belt and comprises mainly of cordierite–biotite granite. To the south of the Darongshan pluton is the Pubei pluton, which is also composed mainly of cordierite–biotite granite. To its southwest is the Taima pluton, which is mainly composed of the orthopyroxene granite porphyry. The Jiuzhou pluton is NE-trending between the Taima and Pubei plutons, and has a length of ~150 km and a width range of 10–30 km. The Jiuzhou pluton is mainly composed of hypersthene–cordierite–biotite adamellite, with coarse-grained porphyritic granite in the central facies and fine-grained granite in the marginal facies. There are abundant enclaves in this pluton. The rock types of the enclaves include granulite, gneiss, biotite-rich gneiss, metasandstone, quartzite, with predominant granulite and gneiss (>90%).

For this study, the granulite enclave samples were collected from the Jiuzhou pluton. The granulite enclaves occur as ellipses or lenses, and are closely associated with the host granite (Fig. 2a, b). They are gray to dark gray and unequal in size, with diameters ranging between several centimeters and 20 cm. Most granulites display crystalloblastic textures and symplectites of orthopyroxene + cordierite and orthopyroxene + plagioclase. The typical mineral assemblage includes orthopyroxene (15–30% in volume), garnet (10–30%), plagioclase (20–30%), K-feldspar (15–20%), biotite (5–30%), quartz (5–15%), cordierite (10–30%), spinel (ca. 5%), sillimanite (0–10%), and Fe–Ti oxides (ca. 5%). Accessories include zircon, apatite, rutile, diaspore and grandidierite.

At least three generations of mineral assemblage were recognized in the granulite enclaves. The first assemblage is biotite + quartz + plagioclase + sillimanite, and only occurs as inclusions in garnet porphyroblasts (Fig. 2c). This represents the prograde metamorphic stage. The peak metamorphic assemblage consists of garnet + orthopyroxene + plagioclase + K-feldspar + biotite + quartz + cordierite + spinel + sillimanite. The mineral assemblage of spinel + quartz in some samples indicates a HT metamorphic history (Fig. 2d and e). The retrograde assemblages are composed of symplectites of orthopyroxene + plagioclase and orthopyroxene + cordierite surrounding the porphyroblastic garnet (Fig. 2f and g), which indicate a rapid decompression event.

3. Analytical techniques

3.1. Electron microprobe analysis

Mineral compositions were determined using a JXA-8100 electron microprobe at the Guangzhou Institute of Geochemistry, Chinese Academy of Sciences (CAS). Analysis conditions consisted of a 15 kV accelerating voltage, a specimen current of 3 nA, and a spot diameter of 2 μm. The analytical errors were generally less than 2%. The representative mineral compositions are listed in Tables 1–7 in the Appendix A.

3.2. Geochemical analysis

Whole-rock major and trace element analysis were performed at the Guangzhou Institute of Geochemistry, CAS. The major element contents were analyzed using wavelength X-ray fluorescence spectrometry (XRF), with analytical errors ≤1%. Trace element abundances of the samples were determined by inductively coupled plasma mass spectrometry (ICP-MS). The analytical techniques were described by Liu et al. (1996). The analytical errors were estimated to be less than 5% for elements >10 ppm and about 10% for transition metals such as Cr, Ni, V, and Sc. Duplicate runs gave <5% RSD (relative standard deviation) for most analyzed elements, with the exception of transition metals, which generally gave <10% RSD. Table 2 displays the analytical results of major and trace element compositions of the granulite enclaves and host granites.

3.3. Sr–Nd isotope analysis

The Sr and Nd isotope ratios were measured at the Guangzhou Institute of Geochemistry, CAS, using a Micromass Isoprobe Multi-Collector Inductively Coupled Plasma Mass Spectrometry (MC-ICP-MS). Measured $^{87}Sr/^{86}Sr$ ratios were normalized to $^{86}Sr/^{88}Sr = 0.1194$ and

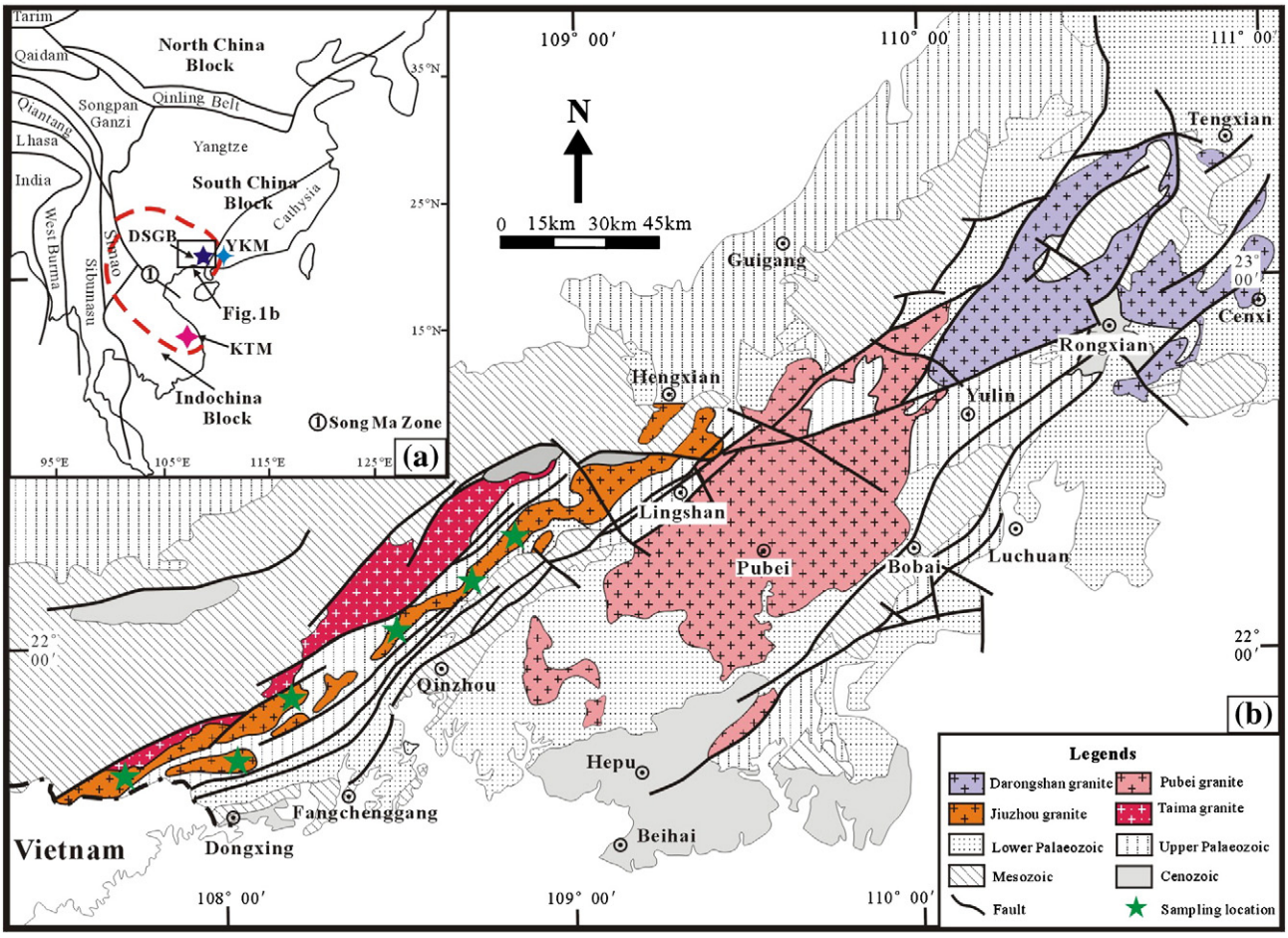

Fig. 1. (a) A simplified tectonic map of Southeast Asia (modified after Chen et al., 2011; Lepvrier and Maluski, 2008; Meng and Zhang, 1999), showing the locations of the Darongshan–Shiwandashan granite belt (DSGB), Kontum massif (KTM), Yunkaidashan Mountain (YKM), and the Emeishan large igneous province (enclosed by the dashed line). (b) A simplified geological map of the DSGB.
Modified from Ma (2002).

$^{143}Nd/^{144}Nd$ ratios were normalized to $^{146}Nd/^{144}Nd = 0.7219$. Analytical errors for Sr and Nd isotopic ratios were given as 2σ. The $^{87}Rb/^{86}Sr$ and $^{147}Sm/^{144}Nd$ ratios were calculated using the Rb, Sr, Sm, and Nd abundances obtained by ICP-MS. Table 3 lists the Sr and Nd isotope compositions of the granulite enclaves.

4. Metamorphic processes

4.1. Metamorphic reactions

In accordance with the mineral assemblages and reaction textures, three stages of metamorphic reactions can be identified in the studied granulite enclaves.

4.1.1. Prograde metamorphic stage

Although the prograde mineral assemblages and microstructures in the granulite enclaves were mostly destroyed due to later peak and retrograde metamorphism, relicts of the prograde history could be locally observed in some of the samples (e.g., 07QZ-1). Garnet is a typical robust mineral that commonly preserves inclusion minerals (Santosh et al., 2007). Minor inclusions of biotite, plagioclase, quartz and sillimanite in porphyroblastic garnets (Fig. 2c) imply that fluid-absent dehydration-melting reactions occurred early in the prograde stage:

$$Bt + Sil + Qtz = Grt + Liq \quad (1)$$

or

$$Bt + Sil + Pl + Qtz = Grt + Kfs + Liq. \quad (2)$$

The appearance of sillimanite inclusions in garnet porphyroblasts suggests that sillimanite was partly involved in the reactions. Both reactions indicated a prograde heating through the stability field of the sillimanite (Brandt et al., 2003).

4.1.2. Peak metamorphic stage

07QZ-1 contains abundant porphyroblastic garnets and needle-like sillimanite with the absence of biotite. This suggests that the temperature for the peak metamorphic stage might exceeded the stability field of biotite. The peak metamorphic stage is marked by the HT assemblage of spinel + quartz occurring between garnets and needle-like sillimanite (Fig. 3b), thus indicating the following reaction:

$$Grt + Sil = Spl + Qtz. \quad (3)$$

4.1.3. Retrograde metamorphic stage

The peak metamorphic mineral assemblages are modified by well-preserved reaction textures, which are diagnostic of retrograde decompression. The retrograde assemblages consist of symplectites of orthopyroxene + plagioclase and orthopyroxene + cordierite surrounding the garnet porphyroblast (Fig. 2f and g). This reflects the breakdown of garnets, as shown in the following two reactions:

$$Grt + Qtz = Opx + Pl \quad (4)$$

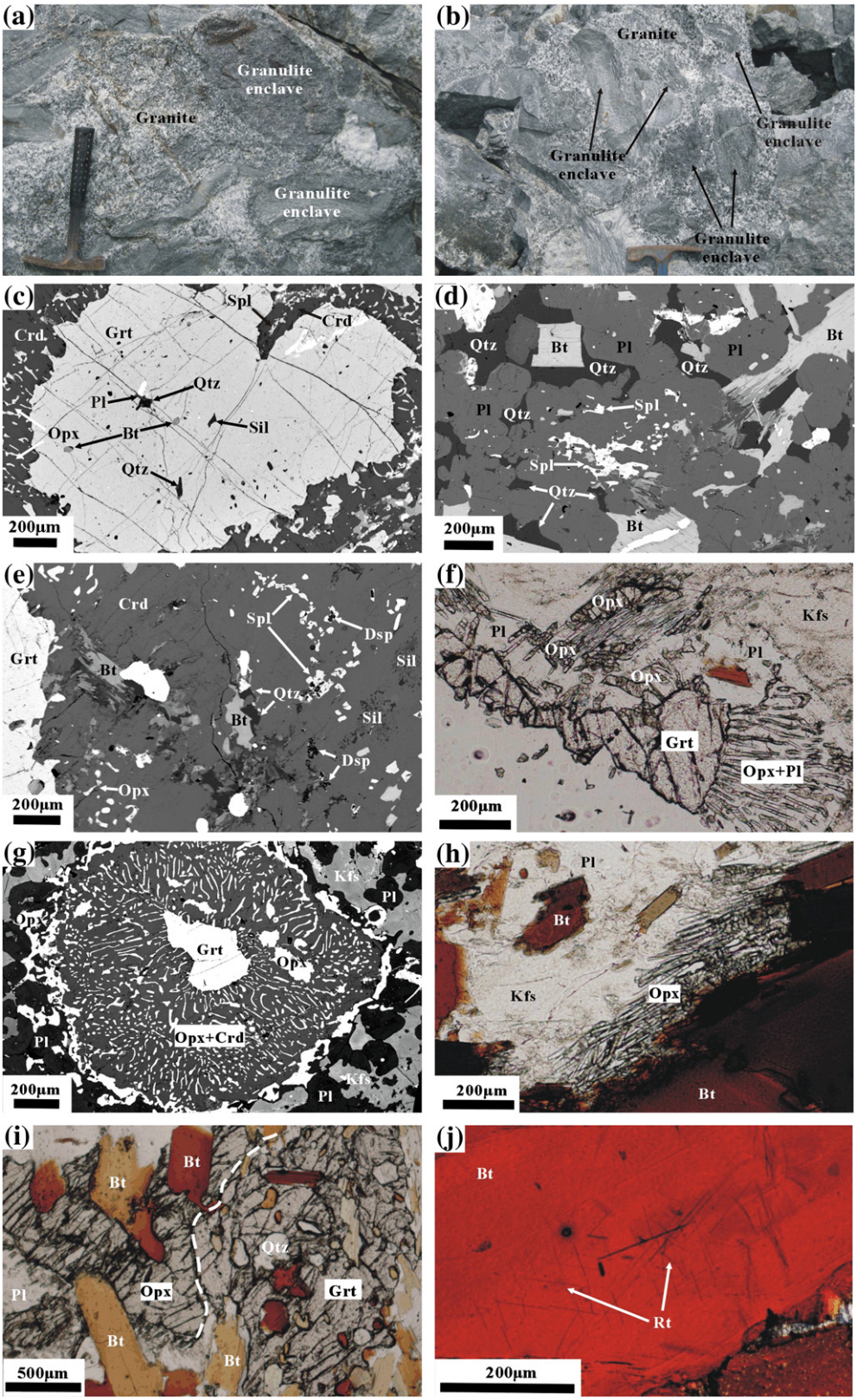

Fig. 2. Field occurrence (a and b) and microphotos (c–j) of the granulite enclaves in the DSGB. In (a) and (b), both the granulite enclaves and the host granites are closely associated with each other. (c) Back-scattered electron (BSE) image of quartz, biotite, plagioclase and sillimanite inclusions in garnet porphyroblast surrounded by symplectic coronae of orthopyroxene + cordierite, indicating the prograde reaction Bt + Sil + Qtz = Grt + L or/and Bt + Sil + Pl + Qtz = Grt + Kf + L. (d) BSE image of mineral assemblage of spinel + quartz + plagioclase + biotite. (e) BSE image of garnet porphyroblast surrounded by cordierite, spinel, quartz, biotite, sillimanite and diaspore. (f) Garnet mantled by symplectite of orthopyroxene + plagioclase (−), indicating the retrograde reaction Grt + Qtz = Opx + Pl. (g) BSE image of garnet mantled by symplectite of orthopyroxene + cordierite, indicating the retrograde reaction Grt + Qtz = Opx + Crd. (h) Biotite rimmed by needle-like orthopyroxene (−), indicating the biotite-dehydration retrograde reaction Bt + Qtz = Opx + Kfs + H_2O. (i) Representative peak metamorphic assemblage of garnet + orthopyroxene + plagioclase + quartz (−). (j) Biotite with needle-like rutile exsolution (−).Mineral abbreviations: garnet — Grt; orthopyroxene — Opx; quartz — Qtz; biotite — Bt; plagioclase — Pl; K-feldspar — Kfs; cordierite — Crd; spinel — Spl; sillimanite — Sil; rutile — Rt; and diaspore — Dsp.

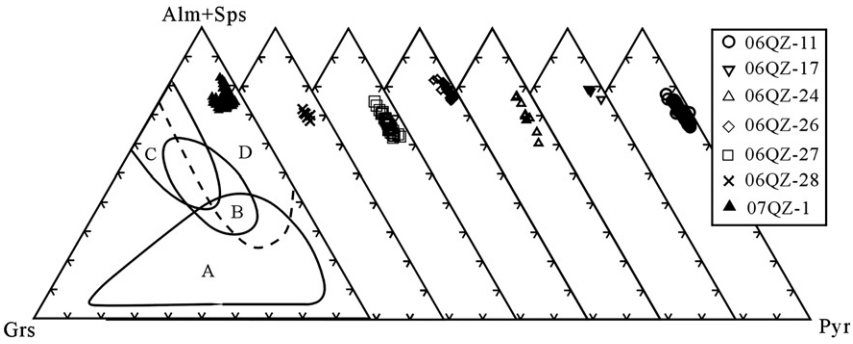

Fig. 3. (Alm + Sps)–Grs–Pyr diagram for garnet of the granulite enclaves from the DSGB (after Lovering and White, 1969). A, B and C are the fields of garnet in eclogites, and D represents the field of garnet in granulites.

$$Grt + Qtz = Opx + Crd. \quad (5)$$

According to Harley (1989), both reactions (4) and (5) are indicative of near-isothermal decompression (ITD), suggesting that the granulite enclaves had undergone rapid exhumation and unroofing during retrograde metamorphism.

The other retrograde texture is biotite rimmed by needle-like orthopyroxenes (Fig. 2h), and indicates the dehydration melting of biotite:

$$Bt + Qtz = Opx + Kfs + H_2O. \quad (6)$$

4.2. Mineral chemistry

4.2.1. Garnet

Garnet is common in the granulite enclaves with biotite, orthopyroxene, quartz and plagioclase inclusions. The garnets are essentially pyrope-almandine solid solution with low spessartine and grossular components (Fig. 3; Appended Table 1). According to the mineral assemblages and reaction textures, the garnets can be classified into two types. Type 1 garnets coexist with orthopyroxene, plagioclase, biotite and quartz free of symplectite (Fig. 2i). The formula for Type 1 garnet is $Prp_{27–32}$, $Alm_{61–64}$, $Grs_{4–5}$, and $Sps_{2–3}$ with insignificant compositional zoning. By contrast, Type 2 garnets are surrounded by the symplectite of orthopyroxene + plagioclase or orthopyroxene + cordierite (Fig. 2f and g). The formula for Type 2 garnet is $Prp_{13–23}$, $Alm_{64–79}$, $Grs_{2–10}$, and $Sps_{3–10}$. Some coarse-grained garnet porphyroblasts show compositional zoning with a gradual decrease of pyrope content and an increase of almandine content from core to rim (Fig. 4). Such chemical zoning in garnet is probably a result of kinetic Fe–Mg diffusion during retrograde metamorphism.

4.2.2. Orthopyroxene

Results of orthopyroxene analysis are listed in Appended Table 2. Orthopyroxenes of the granulite enclaves are dominated by hypersthene (Fig. 5), and can be subdivided into two major generations according to texture. The first generation is euhedral or subhedral crystal with polychroism, and is generally associated with garnet porphyroblast (Fig. 2i), with Wo = 0.18–0.92, En = 40.89–53.32, and Fs = 45.96–58.80. The second generation includes two types. Type 1 orthopyroxene is needle-like, growing around the biotite (Fig. 2h), with Wo = 0.41–0.45, En = 41.27–41.37, and Fs = 58.17–58.32. Type 2 orthopyroxene occurs as fine-grained intergrowth in the orthopyroxene + cordierite symplectite around garnet porphyroblast (Fig. 2g), with Wo = 0.17–0.68, En = 32.71–51.29, and Fs = 48.04–67.00.

4.2.3. Biotite

Results of biotite analysis are listed in Appended Table 3. X_{Mg} values in biotite range between 0.35 and 0.66. The biotites have high TiO_2 contents ranging from 3.25% to 6.72%. Some biotites contain needle-like rutile exsolution (Fig. 2j), indicative of Ti saturation in the metamorphic system. In accordance with the experimental data for Ti solubility in biotite (Patiño Douce, 1993; Patiño Douce et al., 1993), Ti correlated positively with temperature and Al^{VI} in biotite. Some high-Ti biotites that are in equilibrium with a temperature over 950 °C, also indicate a HT metamorphism for the granulite enclaves (Fig. 6).

4.2.4. Cordierite

Cordierite occurs mainly in the matrix of retrograde texture. The coarse-grained cordierite porphyroblasts often contain minor inclusions of zircon and apatite. Appended Table 4 shows the results of cordierite analysis. The FeO and MgO contents of cordierites conspicuously vary in accordance with the textural relationships. The cordierite grains in the matrix have FeO and MgO contents of 6.33–8.98% and 7.31–9.04%, respectively, with an X_{Mg} range of 0.62–0.70. The cordierites involved in symplectites have relatively higher FeO contents (8.20–11.16%) and lower MgO contents (6.10–8.55%), with an X_{Mg} range of 0.51–0.60 (Fig. 7). Because the Fe and Mg contents of cordierite are correlated with pressure, i.e., decreasing pressure results in an increase of Fe and a decrease of Mg (Holdaway and Lee, 1977), the compositional variation between the two cordierite types is consistent with the decompression textures recorded in coexisting garnets.

4.2.5. Spinel

Spinel is common in the studied samples. Spinel occurs either associating with garnet, quartz, and sillimanite (Fig. 2e), or coexisting with quartz, biotite, and plagioclase (Fig. 2d). Analyzed spinels are essentially hercynite–spinel solid solution with an FeO range of 31.32–37.37%, a MgO range of 3.03–6.31%, and a ZnO range of 0.38–3.04% (Appended Table 5). The occurrence of spinel + quartz assemblages in the granulite enclaves indicates a peak metamorphic temperature of over 900 °C.

4.2.6. Feldspars

Feldspars occur as inclusions within garnet and orthopyroxene porphyroblasts, or as euhedral or subhedral grains in the matrix. The feldspar includes K-feldspar and plagioclase, and both are generally chemically heterogeneous (Fig. 8; Appended Table 6). The K-feldspar shows a compositional range of $Or_{74.7–93.8}An_{0–1.1}Ab_{5.9–24.7}$. The plagioclases include albite, oligoclase, andesine, labradorite, bytownite and anorthite, and are dominated by andesine with a formula of $An_{35.4–49.5}Ab_{50.1–66.1}Or_{0.7–8.2}$.

4.2.7. Sillimanite

Sillimanites occur as needle-like aggregates coexisting with spinel, cordierite and garnet (Fig. 2e), or as minor inclusions within garnet cores (Fig. 3c). The aggregate sillimanite shows a SiO_2 range of 34.14–36.28%, and an Al_2O_3 range of 60.15–65.46%. The sillimanite inclusions have SiO_2 and Al_2O_3 contents of 36.28% and 61.04% (Appended Table 7), respectively.

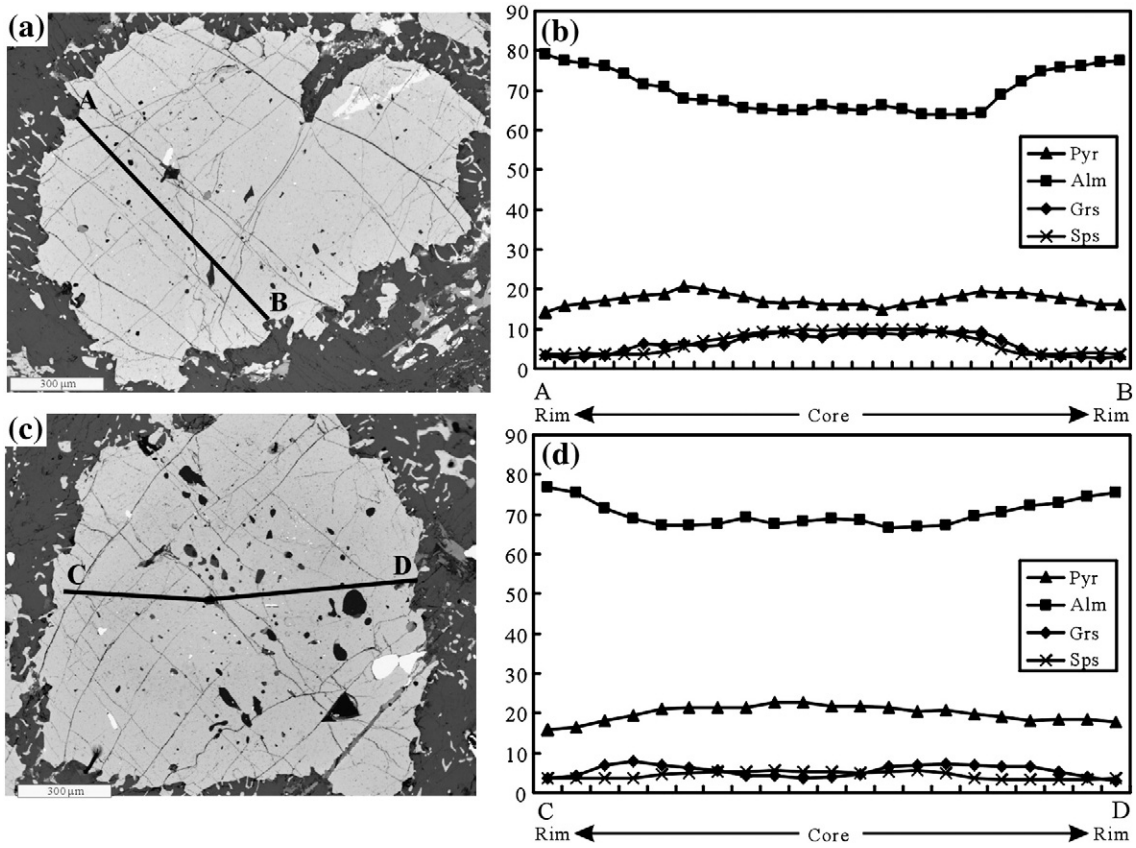

Fig. 4. Composition profiles of the garnet in the granulite enclaves from the DSGB (07QZ-1). Alm — almandine; Sps — spessartine; Pyr — pyrope; and Grs — grossular.

4.2.8. Fe–Ti oxides

Fe–Ti oxides are mostly ilmenite with minor amount of magnetite. Ilmenites have MgO and MnO ranges of 0.01–0.78% and 0.49–2.57%. TiO_2 and Cr_2O_3 contents of magnetite are below 0.10% (Appended Table 7).

4.3. Thermobarometry and P–T path

To calculate the peak metamorphic *P–T* parameters, the chemical compositions of coexisting core portions of porphyroblastic garnet, orthopyroxene, and plagioclase were employed and an iterative method was used. The garnet–orthopyroxene geothermometer and the garnet–orthopyroxene–plagioclase–quartz geobarometer (Bhattacharya et al., 1991) were used in this study. The results yielded a pressure of 7.5–8.0 kbar (26–28 km) and a temperature of 950–1000 °C for peak metamorphism (Table 1), corresponding to a geothermal gradient over 30 °C/km. The estimated temperature range is consistent with both the spinel + quartz assemblage and the existence of the Ti-rich biotite, both of which indicated a peak metamorphic temperature over 900–950 °C.

Retrograde *P–T* conditions were calculated using the composition of the porphyroblastic garnet rim, fine-grained orthopyroxene in the orthopyroxene–cordierite symplectite around garnet, and the plagioclase coexisting with the symplectites. This calculation employed the

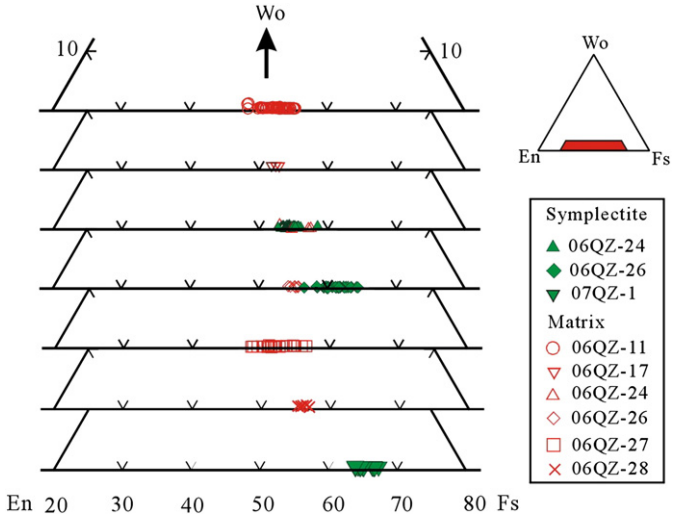

Fig. 5. Wo–En–Fs for orthopyroxene in the granulite enclaves in the DSGB.

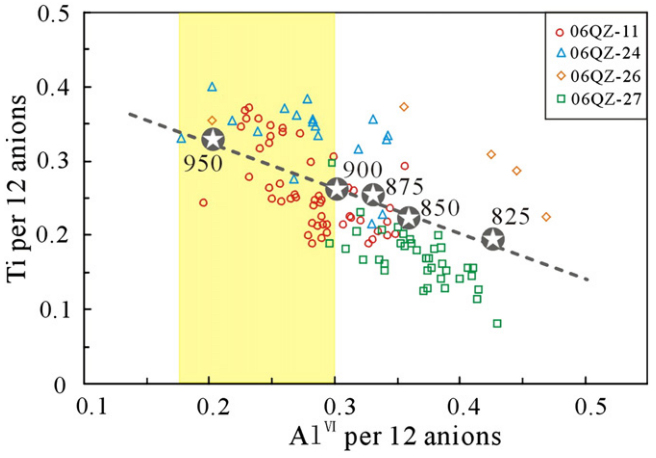

Fig. 6. Correlation between temperature and content of Ti and Al^{VI} in biotite, showing that the Ti content is positively correlated with temperature, whereas the Al^{VI} content is negatively correlated with temperature. The numbers on the line refer to experimental temperatures (Patiño Douce, 1993; Patiño Douce et al. 1993).

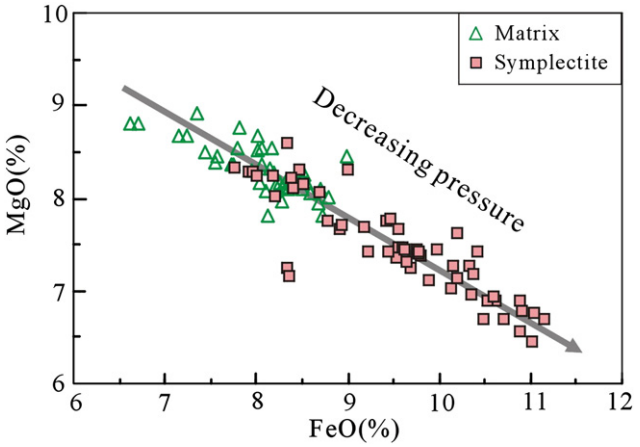

Fig. 7. MgO vs. FeO diagram of the cordierite in the granulite enclaves in the DSGB.

methods of Bhattacharya et al. (1991). The results give a *P–T* condition of 3.2–3.7 kbar and 790–820 °C (Table 1).

The application of conventional geothermobarometry for high- and ultrahigh-temperature granulites may create some uncertainty in estimating *P–T* conditions due to the elemental diffusion between or within minerals during post-peak phase (Fitzsimons and Harley, 1994; Frost and Chacko, 1989; Harley, 1998; Raith et al., 1997). To better estimate the metamorphic conditions, the combined thermobarometric data with petrogenetic grids has been employed (Sajeev and Osanai, 2004; Sajeev et al., 2004). The metamorphic evolution of the studied granulite enclaves favored a petrogenetic grid in a KFMASH (K_2O–FeO–MgO–Al_2O_3–SiO_2–H_2O) system, and its subsystem of FAMS. Fig. 9 shows the portion of the petrogenetic grid for the system KFMASH at low fO_2 (Harley, 1998; Hensen, 1987; Hensen and Harley, 1990), with partial quantification from the experimental data from Bertrand et al. (1991) and Carrington and Harley (1995).

The prograde *P–T* conditions of the granulite enclaves were estimated using the following two aspects: (i) the metamorphic reactions (1) and (2) indicates an initial temperature at around 800 °C (Sengupta et al., 1999); and (ii) the thickness of the Cambrian–Permian sediments ranged from 21 to 25 km (BGMRGX, 1985), corresponding to 6.0–7.0 kbar.

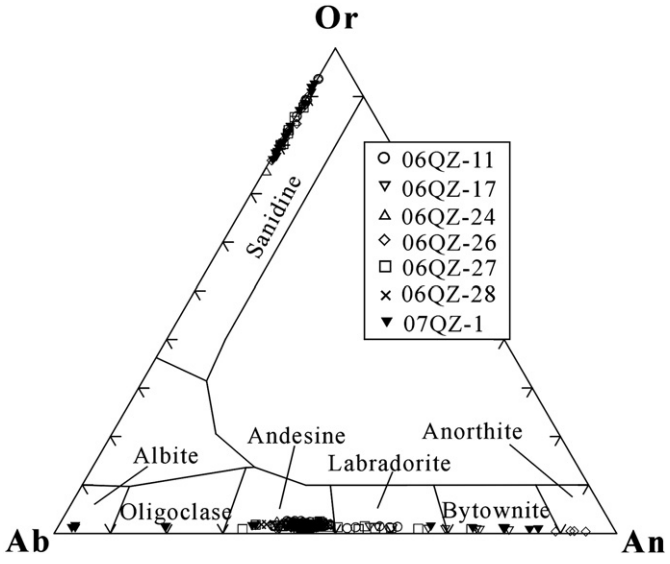

Fig. 8. Ternary classification diagram for feldspar in the granulite enclaves from the DSGB (after Deer et al., 1992). Ab — albite; An — anorthite; and Or — orthoclase.

By combining the prograde, peak and retrograde stages of the metamorphic conditions, we constitute the *P–T* path for the studied granulite enclaves (Fig. 9). The metamorphic evolution started in the stability field of sillimanite, attained its peak stage with the spinel + quartz assemblage and retrograded to the formation of Opx + Pl and Opx + Crd symplectites. This indicated a clockwise near-isothermal decompression *P–T* path (Harley, 1989). Such kind of *P–T* path may reflect an initial crustal thickening and subsequent rapid exhumation history (Ring et al., 1999) in the DSGB. This was probably related to the collision between the SCB and Indochina block during the end of the Permian to Triassic.

5. Whole-rock geochemistry

5.1. Major and trace elements

The granulite enclaves in the DSGB show basic to intermediate compositions with a SiO_2 range of 47.25–63.97%, a MgO range of 2.62–6.99%, an Fe_2O_3 range of 6.88–14.94%, and a $Mg^{\#}$ range of 0.40–0.59 (Table 2). The enclaves have high Al_2O_3 content up to 25.31%, and belong to peraluminous affinities with an A/CNK [Al_2O_3/($CaO + Na_2O + K_2O$) in molecular ratio] range of 1.11–3.14. This is consistent with their high modal Al-rich mineral compositions. According to the discriminant function (D.F.) proposed by Shaw (1972), most of the granulite enclaves have negative D.F. values (Table 9), indicating a sedimentary protolith.

The host granites span a SiO_2 range of 63.41–71.00%, a MgO range of 0.76–2.79%, and a $Mg^{\#}$ range 0.31–0.45 (Table 9). Compared with the granulite enclaves, the host granites have lower Al_2O_3, Fe_2O_3, CaO, TiO_2, and MnO. The host granites have lower A/CNK (1.10–1.26) than those of the granulite enclaves. Most major and trace elements (e.g., MgO, Fe_2O_3, Al_2O_3, TiO_2, MnO, Cr, Ni, V, Ga, Sr, La, and Nb) show negative correlations with SiO_2 from the granulite enclaves to the host granites (Fig. 10), suggesting a cogenetic relationship between the two rock types.

The granulite enclaves show high $\sum$REE contents (234.9–389.6 ppm, Table 2) with the exception of Sample 06QZ-10 (193.3 ppm). They show subparallel chondrite-normalized REE patterns with LREE enrichment to HREE with $La/Yb_{CN} = 6.0–13.9$, and apparently negative Eu anomalies ($Eu/Eu^{*} = 0.38–0.80$). This is similar to that of the average upper continental crust (UCC, Rudnick and Gao, 2003). The investigated host granites have $\sum$REE contents ranging between 190.3 and 382.5 ppm, and show similar chondrite-normalized REE patterns to those of the granulite enclaves with $La/Yb_{CN} = 7.75–12.47$, and $Eu/Eu^{*} = 0.38–0.79$ (Fig. 11a).

In the primitive mantle-normalized spidergrams, the granulite enclaves are characterized by an enrichment of Rb, Ba, Th, Nd, K, Zr, and Hf, and a depletion of Sr, Nb, Ta, P, and Ti (Fig. 11b). These are also similar to the characteristics of UCC. In addition, the enclaves have similar Nd/Ta values (10.65–13.66) to that of UCC (Nb/Ta = 13.33, Rudnick and Gao, 2003). The trace element features of the granulite enclaves suggest that their protoliths could be mainly derived from upper crustal components.

5.2. Sr–Nd isotopes

The granulite enclaves show a measured $^{87}Sr/^{86}Sr$ range of 0.738247–0.760553. The age-corrected $^{87}Sr/^{86}Sr(i)$ at 253 Ma ranges from 0.71295 to 0.74273 (Table 3), which can be subdivided into two groups (Fig. 12a, b). The $^{87}Sr/^{86}Sr(i)$ for samples 06QZ-10 and 06QZ-35-1 is respectively 0.71295 and 0.71346. These values are lower than the others, which have $^{87}Sr/^{86}Sr(i)$ between 0.73031 and 0.74273. The measured $^{143}Nd/^{144}Nd$ for the granulite enclaves ranges from 0.511732 to 0.511918 (Table 3). The calculated $\varepsilon_{Nd}(t)$ at 253 Ma shows a narrow range between −14.8 and −11.2, and a single-stage

Table 1
P–T estimation for the peak and retrograde metamorphic stages of the granulite enclaves using the method proposed by Bhattachaya et al. (1991).

Metamorphic stage	Texture	Grt			Opx			Pl		P(kbar)	T(°C)
		X_{Mg}	α(Pyr)	α(Grs)	X_{Fe}	X_{Mg}	α(En)	X_{An}	α(An)		
Peak	Grt-Opx-Pl-Qtz (cores)	0.32	0.41	0.06	0.51	0.49	0.55	0.44	0.41	7.96	970
		0.32	0.42	0.06	0.52	0.48	0.55	0.44	0.41	8.03	997
		0.31	0.41	0.05	0.52	0.48	0.55	0.44	0.41	7.50	953
		0.32	0.41	0.06	0.51	0.49	0.55	0.57	0.44	7.64	965
		0.32	0.42	0.06	0.51	0.49	0.55	0.60	0.44	7.57	973
Retrograde (symplectite formation)	Grt (rim)-Opx (symplectite) -Pl-Qtz	0.19	0.29	0.03	0.62	0.38	0.45	0.42	0.40	3.59	792
		0.19	0.30	0.02	0.63	0.37	0.45	0.42	0.40	3.23	818
		0.19	0.29	0.03	0.63	0.37	0.45	0.42	0.40	3.69	813
		0.19	0.30	0.02	0.63	0.38	0.45	0.42	0.40	3.21	812
		0.19	0.30	0.02	0.63	0.37	0.45	0.42	0.40	3.27	824

depleted mantle Nd model age (T_{DM}) ranges from 1758 to 2032 Ma (Table 10).

6. Discussion

The granulite enclaves from the DSGB experienced a three-stage metamorphism. They show UCC-type REE patterns, LILE and LREE enrichment, Nb–Ta depletion, and highly evolved Sr–Nd isotopic features. The origins for metamorphic enclaves in granites are various: (1) accidental xenoliths (Mass et al., 1997; Waight et al., 2001); (2) cumulates (Clemens and Wall, 1988; Wall et al., 1987); (3) magma mixing "globules" (Antunes et al., 2009; Didier and Barbarin, 1991; Elburg and Nicholls, 1995; Gomes, 2008; Mass et al., 1997; Silva et al., 2000); and (4) restites (e.g., Chappell et al., 1987; Chen et al., 1989, 1990; White and Chappell, 1977; Williamson et al., 1997). Below, we will discuss the protoliths, origin and the genetic relationship between the granulite enclaves and the host granite, and then address the possible dynamic implications for crustal evolution in the study area.

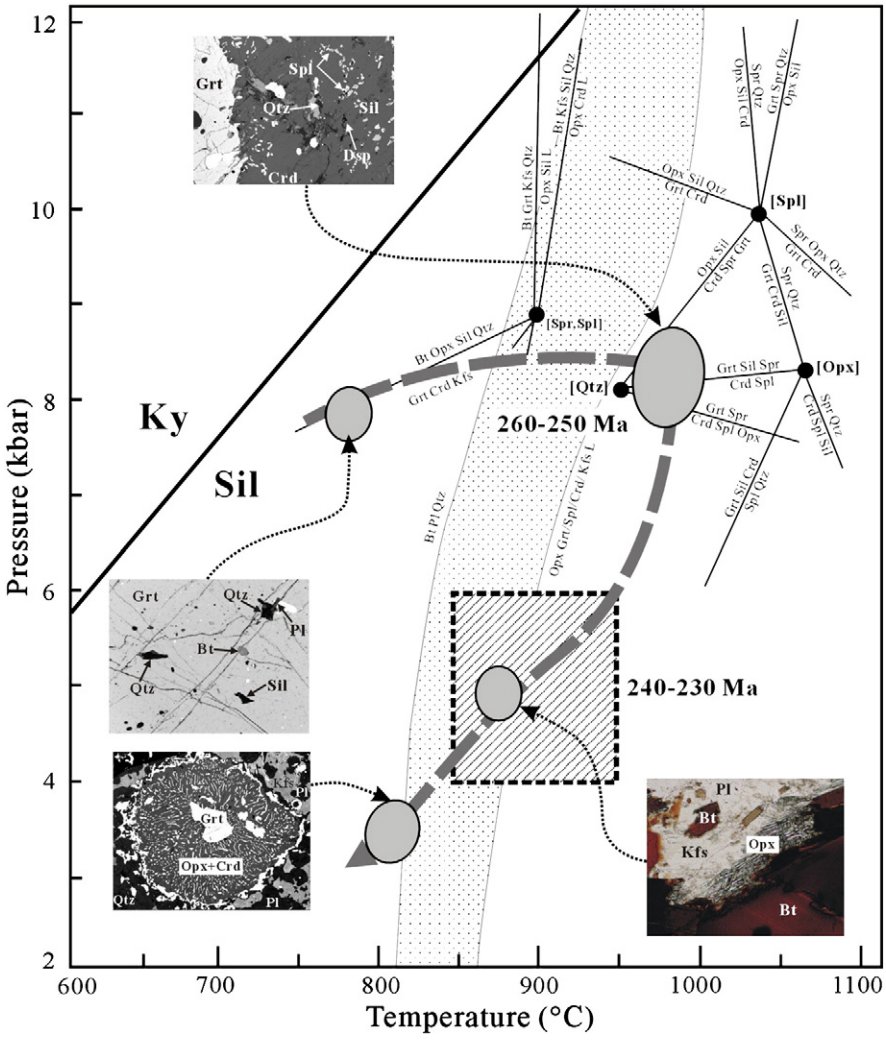

Fig. 9. *P–T* path of the granulite enclaves from the DSGB. The relevant partial petrogenetic grids in the KFMASH and FMAS systems are based on Hensen (1987), Harley (1998), Hensen and Harley (1990), Bertrand et al. (1991) and Carrington and Harley (1995). Also shown is the fluid-absent melting reaction Bt + Pl + Qtz = Opx + Grt/Spl/Crd + Kfs + L (after Vielzeuf and Montel, 1994). The inset photomicrographs show the typical mineral assemblages and reaction textures corresponding to each metamorphic stage. The rectangle refers to the *P–T* condition of granitic magmatism. See details in the text.

Table 2
Representative major oxides (%) and trace element (ppm) compositions of the granulite enclaves and host granites in the DSGB.
After Shaw (1972).

Rock type	Granulite enclave						
Sample	06QZ-10	06QZ-11	06QZ-12	06QZ-13	06QZ-15	06QZ-16-1	06QZ-16-2
SiO_2	57.29	54.89	49.43	50.75	55.27	48.15	57.89
TiO_2	0.69	1.43	1.11	1.13	1.83	1.08	0.90
Al_2O_3	19.10	17.65	21.25	20.91	15.59	21.45	12.35
Fe_2O_3	6.88	10.96	10.08	10.79	11.92	9.16	14.94
MnO	0.06	0.16	0.13	0.14	0.15	0.09	0.17
MgO	2.62	5.00	4.89	5.01	5.04	6.53	5.08
CaO	6.47	3.29	3.77	3.70	3.69	5.30	2.22
Na_2O	2.05	2.20	2.19	2.23	2.11	3.04	1.60
K_2O	2.93	3.26	6.30	4.12	2.91	4.19	3.61
P_2O_5	0.08	0.12	0.06	0.17	0.25	0.19	0.13
LOI	1.46	0.86	0.64	0.72	0.79	0.24	0.78
Total	99.64	99.81	99.85	99.66	99.56	99.43	99.65
$Mg^{\#}$	43.24	47.71	49.23	48.14	45.84	58.77	40.49
A/CNK	1.11	1.40	1.28	1.47	1.23	1.17	1.21
D.F.	1.99	−2.36	1.05	−0.73	−2.86	0.91	−5.49
Sc	15.69	29.54	25.09	25.57	26.79	24.32	30.72
Ti	3718.6	7059	6945	6723	10822	6492	5216.7
V	135.8	184.7	179.4	177	204.9	178.7	176.2
Cr	92.96	184.9	188.9	159.1	142.2	157.5	137
Mn	390.5	1130	1059	1033	1199	626	1299
Co	15.79	47.05	28.24	27.17	27.85	25.72	58.28
Ni	50.84	77.61	75.43	52.5	51.98	62.19	204.4
Cu	164.8	50.57	6.63	8.35	22.93	5.64	210.2
Zn	133.7	120.6	153.4	191.5	173.8	154.3	155.7
Ga	24.2	23.34	29.59	28.54	23.91	29.5	18.72
Ge	2.524	2.33	2.79	2.77	2.69	3.01	2.852
Rb	156	115.9	270.0	160.6	113.0	227.8	134.8
Sr	413.2	193.9	214.4	202.1	196	209	132.2
Y	22.63	42.63	29.64	43.52	41.72	35.1	35.06
Zr	146.6	365.7	201.8	193.3	298	235.6	181
Nb	12.99	18.55	21.47	17.72	26.22	18.2	13.68
Cs	8.991	6.60	8.80	5.47	3.73	6.81	5.576
Ba	928.9	1650	2000	1751	1402	1315	1769
La	44.17	71.62	61.43	73.1	56.03	61.53	49.28
Ce	80.42	135.6	117.2	139.8	109.2	119.6	94.28
Pr	9.306	16.34	13.43	16.47	13.01	13.89	11.26
Nd	35.08	62.07	49.25	62.74	51.56	52.46	43.16
Sm	6.129	11.33	8.56	11.70	9.93	9.53	8.035
Eu	1.433	2.36	2.07	2.60	2.47	1.97	1.626
Gd	5.349	10.30	7.34	10.45	9.26	8.48	7.309
Tb	0.766	1.55	1.04	1.53	1.44	1.26	1.117
Dy	4.4	8.84	6.04	8.95	8.48	7.30	6.792
Ho	0.882	1.80	1.20	1.92	1.77	1.45	1.451
Er	2.349	5.07	3.22	5.72	4.71	3.78	4.291
Tm	0.354	0.77	0.47	0.87	0.70	0.54	0.7
Yb	2.33	5.00	3.16	5.99	4.44	3.46	4.806
Lu	0.371	0.81	0.52	0.98	0.69	0.54	0.77
Hf	3.867	10.83	5.92	5.66	8.01	6.68	5.36
Ta	0.904	1.56	1.94	1.53	2.02	1.69	1.163
Pb	24.54	28.11	66.61	41.36	26.74	27.44	30.03
Th	15.39	29.09	28.78	30.42	21.21	24.01	23.19
U	2.845	4.29	4.16	3.88	2.54	5.26	3.623
La/Yb_{CN}	13.6	10.27	13.94	8.76	9.06	12.76	7.36
$\sum$ REE	193.3	333.4	274.9	342.8	273.7	285.8	234.9
LREE/HREE	10.51	8.77	10.95	8.42	7.69	9.66	7.62
Eu/Eu*	0.77	0.67	0.80	0.72	0.79	0.67	0.65

Rock type	Granulite enclave						
Sample	06QZ-17	06QZ-20	06QZ-21	06QZ-23	06QZ-24	06QZ-25	06QZ-26
SiO_2	47.40	60.26	58.89	57.00	49.02	57.10	47.25
TiO_2	1.17	1.21	1.16	1.03	1.28	1.36	1.36
Al_2O_3	23.20	15.03	16.08	17.46	22.15	16.23	25.31
Fe_2O_3	14.50	10.80	11.06	9.42	12.84	10.84	13.21
MnO	0.48	0.15	0.13	0.13	0.19	0.17	0.23
MgO	6.13	4.79	4.04	4.24	6.99	4.93	5.96
CaO	2.74	3.15	3.17	3.63	1.98	4.12	2.20
Na_2O	1.57	1.90	1.85	2.41	1.28	2.02	1.39
K_2O	1.26	2.45	2.33	3.26	2.14	2.09	1.98
P_2O_5	0.14	0.12	0.09	0.11	0.13	0.16	0.13
LOI	1.01	0.39	0.97	0.87	1.63	1.05	0.56
Total	99.60	100.25	99.77	99.56	99.64	100.06	99.57

(continued on next page)

Table 2 (*continued*)

Rock type	Granulite enclave						
Sample	06QZ-17	06QZ-20	06QZ-21	06QZ-23	06QZ-24	06QZ-25	06QZ-26
$Mg^{\#}$	45.82	47.01	42.20	47.36	52.12	47.62	47.44
A/CNK	2.74	1.37	1.49	1.30	2.88	1.31	3.14
D.F.	−5.22	−4.19	−3.37	−1.13	−6.29	−3.16	−4.82
Sc	51.61	26.21	21.96	23.1	35.51	34.12	26.5
Ti	7133	7195	6773	6153	7706	8090	7890
V	213.7	173.1	157.4	159.5	227.8	219.5	190.2
Cr	149.8	166.9	151.3	142	211.3	209.3	156.4
Mn	3692	1169	988	973	1584	1817	1328
Co	66.23	23.92	32.31	22.6	61.05	33.08	26.47
Ni	59.16	47.68	96.94	55.81	38.03	43.6	46.96
Cu	43.51	30.52	134.40	34.80	6.38	8.84	27.41
Zn	142.7	134.1	145.1	125.5	292.7	238.1	164.3
Ga	32.79	21.73	22.87	24.31	37.72	37.83	22.8
Ge	3.84	2.96	1.71	2.68	2.22	3.13	2.24
Rb	55.9	102.8	110.0	126.5	96.2	69.0	67.3
Sr	113.6	148.5	154.6	190.9	126.3	126.1	172.1
Y	80.7	34.91	26.6	37.73	46.45	49.28	30.69
Zr	231.7	314.3	338	226.6	281.6	245.7	253.6
Nb	16.24	17.5	18.57	15.9	19.12	20.69	18.71
Cs		5.22	6.30	4.82		3.87	3.17
Ba	586	676	421	1079	703	1454	884
La	72.55	50.39	60.52	62.55	68.48	69.99	51.99
Ce	142.8	96.96	116.1	119.1	138	137.2	99.89
Pr	17.14	11.42	13.78	13.78	16.52	16.52	11.74
Nd	64.8	43.16	51.48	52.52	60.69	63.46	44.86
Sm	11.86	8.05	9.11	9.57	11.06	12.05	8.29
Eu	1.69	1.83	1.66	2.21	1.29	1.92	1.75
Gd	10.21	7.36	7.80	8.75	9.57	10.84	7.40
Tb	1.79	1.14	1.03	1.30	1.51	1.62	1.07
Dy	12.71	6.97	5.73	7.75	8.85	10.13	6.09
Ho	3.04	1.42	1.15	1.59	1.77	2.12	1.22
Er	8.83	4.20	3.14	4.43	4.91	5.91	3.41
Tm	1.39	0.66	0.50	0.66	0.73	0.88	0.52
Yb	8.63	4.39	3.38	4.39	4.72	5.73	3.61
Lu	1.28	0.72	0.54	0.68	0.72	0.90	0.58
Hf	5.30	8.99	9.19	6.52	6.64	7.24	6.47
Ta	1.34	1.47	1.52	1.31	1.40	1.81	1.42
Pb	12.13	23.02	19.98	30.29	12.15	18.27	20.93
Th	26.73	22.07	26.71	28.46	30.28	31.19	21.81
U	2.88	3.58	3.13	3.81	3.57	4.03	2.12
La/Yb_{CN}	6.03	8.23	12.84	10.23	10.40	8.76	10.34
$\sum$ REE	358.7	238.7	275.9	289.3	328.8	339.3	242.4
LREE/HREE	6.49	7.88	10.85	8.79	9.03	7.90	9.14
Eu/Eu^{*}	0.47	0.72	0.60	0.74	0.38	0.51	0.68

Rock type	Granulite enclave					Granite	
Sample	06QZ-27-1	06QZ-29	06QZ-31	06QZ-32-2	06QZ-35-1	06QZ-2	06QZ-3
SiO_2	54.98	50.11	49.27	61.41	48.97	65.72	71.00
TiO_2	1.25	1.02	1.45	1.00	1.06	0.95	0.48
Al_2O_3	16.74	22.19	19.50	14.45	23.98	14.21	13.23
Fe_2O_3	12.04	8.54	13.42	9.90	9.18	6.75	3.34
MnO	0.18	0.09	0.19	4.07	0.06	0.10	0.05
MgO	5.19	4.57	5.79	0.13	4.43	2.03	0.76
CaO	3.32	4.10	4.26	3.35	1.98	3.08	1.41
Na_2O	2.00	2.34	2.46	2.07	1.17	2.20	2.38
K_2O	2.68	5.75	2.46	2.16	7.40	3.56	5.31
P_2O_5	0.12	0.12	0.19	0.12	0.11	0.16	0.11
LOI	1.14	0.79	0.58	1.03	1.29	1.07	1.89
Total	99.64	99.62	99.57	99.68	99.62	99.83	99.95
$Mg^{\#}$	46.32	51.68	46.32	45.14	49.11	37.57	31.15
A/CNK	1.44	1.32	1.42	1.28	1.82	1.17	1.10
D.F.	−3.47	1.76	−2.19	−3.27	−0.04		
Sc	29.23	23.42	33.09	21.06	29.56	14.37	5.776
Ti	7161	6213	8339	5706.1	5590	5427	2531.5
V	171.5	169.6	203.4	140.5	183.6	82.24	29.17
Cr	156.5	145.1	179.9	133.5	172.8	41.27	18.39
Mn	1395	777	1523	993.2	575	713	337.8
Co	25.92	35.4	30.68	29.55	54.62	13.5	4.821
Ni	50.59	60.33	61.02	83.64	82.91	20.89	3.268
Cu	31.36	2.46	24.56	83.89	4.65	25.87	11.97
Zn	179.4	121.7	180.1	126.7	136.1	106.4	59.53
Ga	23.03	30.27	29.47	20.76	39.01	18.73	18.28
Ge	2.20	2.41	2.77	2.48	2.43	2.02	1.579
Rb	97.7	207.9	110.7	84.1	456.0	156.3	284.9

Table 2 (*continued*)

Rock type	Granulite enclave					Granite	
Sample	06QZ-27-1	06QZ-29	06QZ-31	06QZ-32-2	06QZ-35-1	06QZ-2	06QZ-3
Sr	173.1	282	190	165.7	99.8	133.2	60.63
Y	35.33	36.34	62.06	29.38	42.81	38.64	42.06
Zr	236.7	184.8	301.4	210.5	148	332.5	324.2
Nb	17.3	18.33	22.23	14.54	19.69	16.9	12.43
Cs	4.35		3.62	3.631		15.49	14.83
Ba	1279	1668	849	672.6	1753	780	669.3
La	60.71	61.74	82.68	56.79	65.26	61.12	45.86
Ce	116.2	120.9	156.2	107.7	122.8	114.4	89.61
Pr	13.42	13.99	18.64	12.56	14.72	13.55	10.36
Nd	51.44	50.38	70.29	48.07	51.66	51	39.83
Sm	9.32	8.81	13.13	8.764	8.34	9.33	7.994
Eu	2.17	1.79	2.68	1.986	1.44	1.49	0.982
Gd	8.37	7.62	12.71	7.884	7.56	8.64	7.962
Tb	1.20	1.20	2.00	1.065	1.38	1.28	1.34
Dy	7.29	6.72	12.32	6.039	7.95	7.37	8.137
Ho	1.45	1.31	2.58	1.223	1.62	1.49	1.689
Er	4.15	3.62	7.20	3.383	4.53	4.06	4.627
Tm	0.62	0.51	1.07	0.527	0.65	0.61	0.688
Yb	4.24	3.22	6.99	3.515	4.03	3.88	4.244
Lu	0.65	0.52	1.09	0.588	0.61	0.60	0.63
Hf	6.65	4.35	8.36	5.887	4.19	8.23	8.143
Ta	1.28	1.72	1.76	1.218	1.67	1.42	1.212
Pb	23.01	55.88	21.85	21.42	31.29	27.16	30.78
Th	27.65	22.63	36.27	24.24	24.23	26.45	30.01
U	2.85	3.51	3.64	2.907	4.80	3.77	6.586
La/Yb_{CN}	10.28	13.74	8.48	11.59	11.63	11.44	7.75
$\sum$ REE	281.2	282.3	389.6	235.9	292.5	260.59	223.95
LREE/HREE	9.05	10.42	7.48	9.74	9.33	9.25	6.64
Eu/Eu*	0.75	0.67	0.63	0.73	0.55	0.54	0.38

Rock type	Granite						
Sample	06QZ-5	06QZ-6	06QZ-21-2	06QZ-33	06QZ-35-2	06QZ-41	06QZ-42
SiO_2	67.04	68.90	63.41	63.98	63.78	66.63	66.63
TiO_2	0.83	0.62	0.71	0.98	0.97	0.93	0.85
Al_2O_3	14.51	12.96	15.61	14.82	14.89	14.20	14.65
Fe_2O_3	5.85	6.87	6.57	7.73	7.71	6.73	6.04
MnO	0.07	0.10	0.09	0.11	0.09	0.09	0.08
MgO	1.71	2.26	2.74	2.79	2.50	2.06	1.87
CaO	3.10	4.38	2.66	3.58	4.38	3.02	2.97
Na_2O	2.14	1.67	2.21	2.18	2.37	1.99	2.12
K_2O	3.81	1.31	4.07	3.14	1.86	3.61	3.89
P_2O_5	0.16	0.16	0.10	0.15	0.19	0.15	0.15
LOI	0.54	1.09	1.42	0.70	1.02	0.66	0.86
Total	99.74	100.33	99.59	100.15	99.75	100.05	100.11
$Mg^{\#}$	36.87	39.68	45.44	41.87	39.32	37.92	38.20
A/CNK	1.16	1.14	1.26	1.15	1.13	1.13	1.14
D.F.							
Sc	12.96	12.98	14.69	19.38	26.39	15.08	13.4
Ti	4354	3427.5	3671.2	5940.9	7766	5446	4724
V	71.49	108.7	89.56	106.4	158.4	88.23	77.03
Cr	41.23	67.16	85.31	82.41	97.84	59.1	47.09
Mn	573	749.6	667.1	838.5	1000.8	675	612
Co	11.24	15.55	14.62	16	68.34	13.93	12.53
Ni	17.15	32.69	32.04	33.33	49.23	24.05	19.76
Cu	22.39	32.69	31.35	38.46	64.9	30.86	20.96
Zn	85.4	95.92	95.52	105.2	138.5	105.2	94.34
Ga	18.58	16.79	19.97	20.06	30.19	19.62	20.24
Ge	1.97	1.641	2.184	2.361	2.805	2.30	2.09
Rb	156.2	67.38	134.9	110	102.2	161	163.6
Sr	119.6	136.1	165	187.1	212.1	124	147.5
Y	34.49	24.16	29.71	32.24	52.08	32.44	31.1
Zr	381.4	214.4	189.9	454.4	443.9	341.2	297.9
Nb	14.93	7.937	11.89	15.43	21.32	15.83	14.95
Cs	8.63	6.359	6.125	4.248		10.22	9.33
Ba	847	593.9	1133.3	1216.7	278	762	908
La	57.63	42.69	55.53	61.11	80.31	56.29	53.33
Ce	108.6	77.76	105.6	115.5	160.6	107.5	100
Pr	12.65	9.14	12.32	13.26	19.23	12.69	11.57
Nd	47.76	34.95	45.75	51.02	70.16	48.27	43.55
Sm	8.76	6.147	8.173	9.181	12.98	8.93	7.99
Eu	1.49	1.545	1.84	2.226	2.365	1.50	1.55
Gd	7.98	5.765	7.158	8.074	11.42	8.05	7.49
Tb	1.17	0.801	1.061	1.141	1.733	1.14	1.10

(*continued on next page*)

Table 2 (*continued*)

Rock type	Granite						
Sample	06QZ-5	06QZ-6	06QZ-21-2	06QZ-33	06QZ-35-2	06QZ-41	06QZ-42
Dy	7.08	4.59	6.09	6.595	9.848	6.65	6.44
Ho	1.41	0.963	1.225	1.307	1.932	1.32	1.28
Er	3.87	2.619	3.341	3.684	5.271	3.62	3.51
Tm	0.58	0.374	0.505	0.552	0.776	0.55	0.51
Yb	3.75	2.509	3.195	3.737	5.04	3.53	3.32
Lu	0.58	0.402	0.496	0.599	0.801	0.56	0.54
Hf	9.70	5.544	5.262	11.58	9.815	8.48	8.17
Ta	1.31	0.598	1.061	1.295	1.675	1.38	1.35
Pb	28.94	18.72	32.92	29.96	26.09	26.43	29.21
Th	26.78	12.45	25.32	27.12	30.93	25.70	24.67
U	4.07	0.899	4.431	3.154	3.274	3.60	3.79
La/Yb_{CN}	11.54	12.2	12.47	11.73	11.43	11.31	11.01
$\sum$REE	242.16	190.26	252.28	277.99	382.47	278.81	263.30
LREE/HREE	9.02	9.56	9.94	9.82	9.39	8.98	8.97
Eu/Eu*	0.61	0.79	0.74	0.79	0.59	0.51	0.54

Note: D.F. = $10.44 - 0.21SiO_2 - 0.32\ Fe_2O_3$ (total Fe) $- 0.98MgO + 0.55CaO + 1.46Na_2O + 0.54K_2O$.

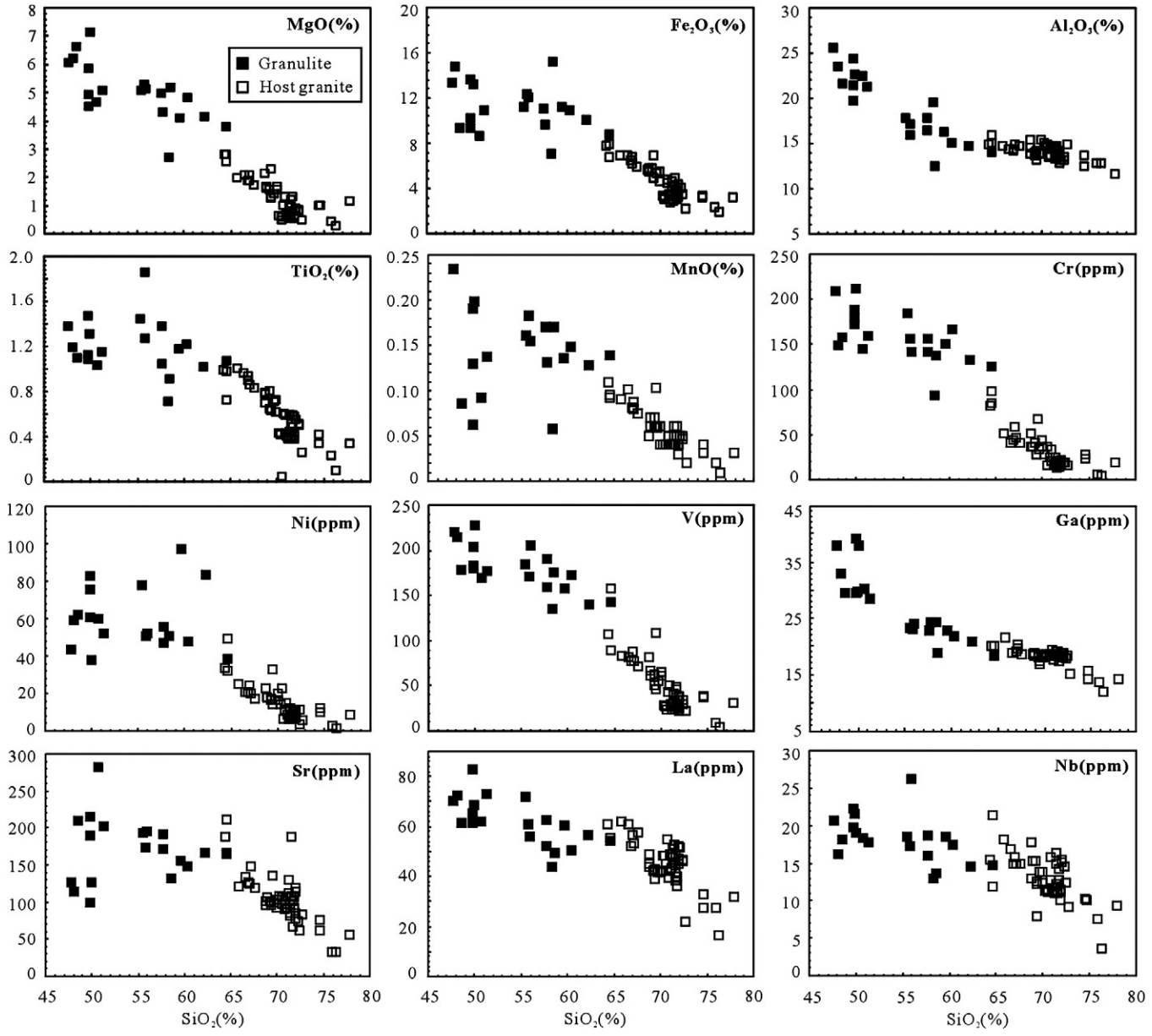

Fig. 10. Harker diagrams for the granulite enclaves and host granites in the DSGB. Data sources: the granulite enclaves — this study; the host granites — Deng (2003) and this study.

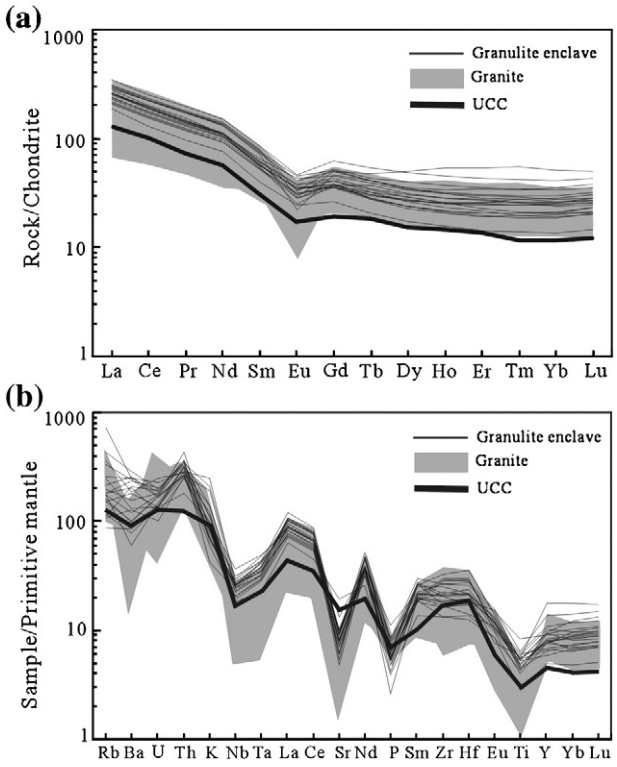

Fig. 11. Chondrite-normalized rare earth element (REE) patterns (a), and primitive mantle normalized trace element spidergrams (b) of the granulite enclaves in the DSGB. Data for the host granites are from this study and Deng (2003). Data for UCC are from Rudnick and Gao (2003). Chondrite and primitive normalized values are from Sun and McDonough (1989).

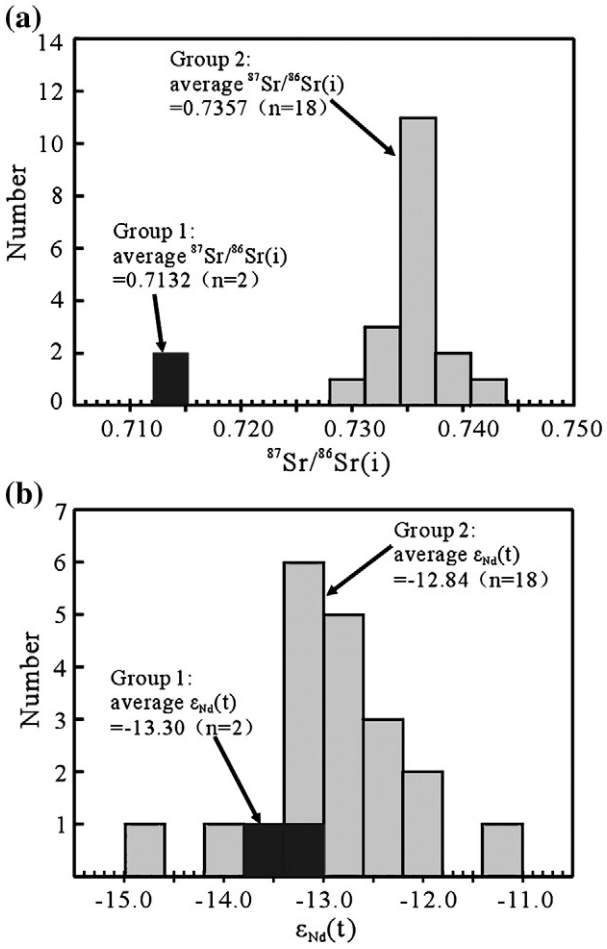

Fig. 12. Histograms of $^{87}Sr/^{86}Sr(i)$ (a), and $\varepsilon_{Nd}(t)$ (b) of the granulite enclaves in the DSGB.

6.1. Protoliths for the granulite enclaves

As discussed earlier, the high Al_2O_3, high A/CNK, and negative D.F. value in most of the studied granulite enclaves are indicatives of sedimentary protoliths. Also, with the exception of 06QZ-10, the rest of the enclaves plot close to the pelitic end-member in the pelitic–psammitic sedimentary rock field in the (al + fm)–(c + alk) vs. si diagram (Fig. 14, Winker, 1967), suggesting that most of the enclaves were metapelites. This is consistent with their UCC-like REE patterns and trace element spidergrams.

The dominant source protoliths of these granulite enclaves developed more evolved Sr and Nd isotopic compositions (Fig. 13) compared with the typical granodiorite and its enclaves from the Lachlan Fold Belt in Australia (Collins, 1996; King et al., 1997; McCulloch and Chappell, 1982). These isotopic features are consistent

Table 3
Sr–Nd isotopic compositions of the granulite enclaves in the DSGB.

Sample	Rb (ppm)	Sr (ppm)	$^{87}Rb/^{86}Sr$	$^{87}Sr/^{86}Sr$	2σ	$^{87}Sr/^{86}Sr(i)$	Sm (ppm)	Nd (ppm)	$^{147}Sm/^{144}Nd$	$^{143}Nd/^{144}Nd$	2 σ	age	ε_{Nd} (0)	ε_{Nd} (t)	T_{DM} /Ma	$f_{Sm/Nd}$
06QZ-10	156.00	413.20	1.093	0.717393	0.000014	0.7135	6.13	35.08	0.105615	0.511790	0.000008	253	−16.5	−13.6	1912	−0.46
06QZ-11	115.90	193.90	1.730	0.741429	0.000016	0.7352	11.33	62.07	0.110343	0.511857	0.000007	253	−15.2	−12.5	1901	−0.44
06QZ-12	270.00	214.40	3.646	0.755851	0.000015	0.7427	8.56	49.25	0.105017	0.511812	0.000007	253	−16.1	−13.2	1871	−0.47
06QZ-13	160.60	202.10	2.301	0.745447	0.000016	0.7372	11.70	62.74	0.112730	0.511830	0.000007	253	−15.8	−13.1	1986	−0.43
06QZ-14	74.90	166.90	1.299	0.740164	0.000018	0.7355	8.67	47.03	0.111388	0.511832	0.000008	253	−15.7	−13.0	1957	−0.43
06QZ-15	113.00	196.00	1.669	0.742019	0.000013	0.7360	9.93	51.56	0.116445	0.511849	0.000007	253	−15.4	−12.8	2032	−0.41
06QZ-16-1	227.80	209.00	3.155	0.747062	0.000018	0.7357	9.53	52.46	0.109780	0.511918	0.000007	253	−14.0	−11.2	1802	−0.44
06QZ-16-2	134.80	132.20	2.952	0.744287	0.000016	0.7337	8.04	43.16	0.112538	0.511873	0.000007	253	−14.9	−12.2	1918	−0.43
06QZ-17	55.91	113.60	1.425	0.740495	0.000013	0.7354	11.86	64.80	0.110638	0.511864	0.000007	253	−15.1	−12.3	1896	−0.44
06QZ-21-1	110.00	154.60	2.060	0.738847	0.000013	0.7314	9.11	51.48	0.106962	0.511732	0.000009	253	−17.7	−14.8	2018	−0.46
06QZ-23	126.50	190.90	1.918	0.740879	0.000013	0.7340	9.57	52.52	0.110173	0.511819	0.000008	253	−16.0	−13.2	1953	−0.44
06QZ-24	96.21	126.30	2.205	0.738247	0.000015	0.7303	11.06	60.69	0.110163	0.511846	0.000007	253	−15.4	−12.7	1914	−0.44
06QZ-26	68.99	126.10	1.584	0.74012	0.000015	0.7344	12.05	63.46	0.114785	0.511886	0.000008	253	−14.7	−12.0	1942	−0.42
06QZ-27-1	97.65	173.10	1.633	0.740469	0.000018	0.7346	9.32	51.44	0.109477	0.511815	0.000007	253	−16.1	−13.2	1946	−0.44
06QZ-29	207.90	282.00	2.134	0.747547	0.000015	0.7399	8.81	50.38	0.105698	0.511816	0.000007	253	−16.0	−13.1	1877	−0.46
06QZ-31	110.70	190.00	1.687	0.741706	0.000019	0.7356	13.13	70.29	0.112919	0.511838	0.000008	253	−15.6	−12.9	1978	−0.43
06QZ-32-1	14.42	102.90	0.406	0.738821	0.000013	0.7374	6.30	31.13	0.122395	0.511908	0.000008	253	−14.2	−11.8	2066	−0.38
06QZ-32-2	84.10	165.70	1.469	0.740697	0.000012	0.7354	8.76	48.07	0.110211	0.511822	0.000008	253	−15.9	−13.1	1950	−0.44
06QZ-35-1	456.00	99.80	13.228	0.760553	0.000018	0.7129	8.34	51.66	0.097614	0.511808	0.000007	253	−16.2	−13.0	1758	−0.50
06QZ-37	24.94	135.00	0.535	0.740752	0.000018	0.7388	6.24	32.28	0.116911	0.511790	0.000008	253	−16.5	−14.0	2134	−0.41

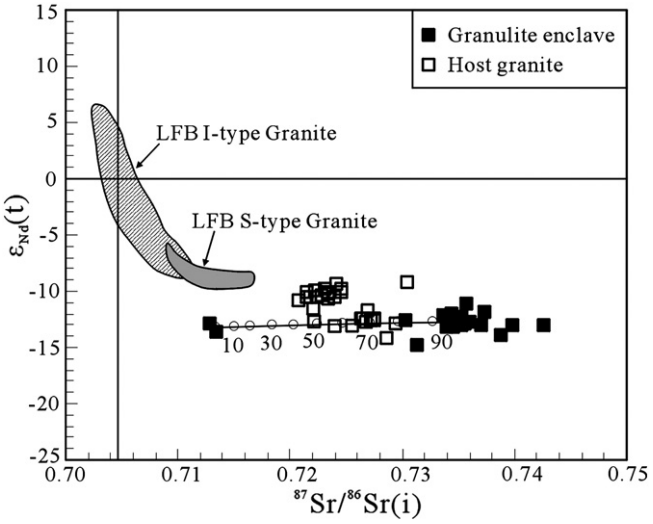

Fig. 13. $^{87}Sr/^{86}Sr(i)$ vs. $\varepsilon_{Nd}(t)$ diagram of the granulite enclaves and the host granites in the DSGB and comparison with the LFB S-type and I-type granites (Collins, 1996; King et al., 1997; McCulloch and Chappell, 1982). The mixing line denotes the possible components involved in the melting source of the granites. Calculation parameters are: the low-$^{87}Sr/^{86}Sr(i)$ granulite has Sr = 256.5 ppm, $^{87}Sr/^{86}Sr(i) = 0.7132$, and $\varepsilon_{Nd}(t) = -13.30$; and the high-$^{87}Sr/^{86}Sr(i)$ granulite has Sr = 170.8 ppm, $^{87}Sr/^{86}Sr(i) = 0.7357$, and $\varepsilon_{Nd}(t) = -12.84$. The Sr and Nd data of the host granites are from Qi et al. (2007), and Hsieh et al. (2008).

with our previously reported zircon Hf isotopic compositions (Zhao et al., 2010). All these features indicate that the granulite enclave protoliths could have originated from upper continental crust.

6.2. Origin of the granulite enclaves

The metasedimentary origin for the studied granulite enclaves precludes the cumulate and magma mixing models. Based on field observations — the distinct lithologic features between the granulite enclaves and the country rocks (e.g., slates, sandshales, carbonates etc.) of the granites, the granulite enclaves are unlikely the accidental xenoliths from the wall rocks. We therefore consider a restite origin for them.

In the restite model, the systematic linear chemical variations of most granitoid suites could be explained by the progressive separation of restite and melt during magma transportation (Chappell et al., 1987; White and Chappell, 1977). Such restites are usually recognized as metasedimentary enclaves in S-types, and mafic hornblende-rich enclaves in I-type granitoids (White and Chappell, 1977). The

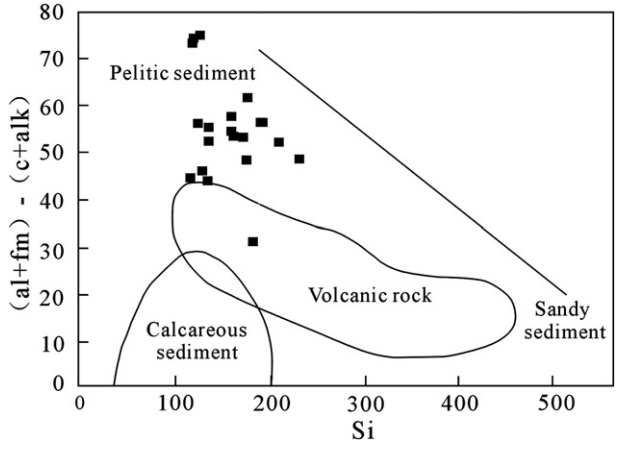

Fig. 14. Plots of (al + fm)–(c + alk) vs. si diagram of the granulite enclaves in the DSGB for constraining the possible protoliths.
After Winker (1967).

similar REE and trace element patterns (Fig. 11), together with the linear correlations between most elements and SiO_2 (Fig. 10) in the studied granulite enclaves and the host granites favor the restite model. In the following section, we employ the available Sr–Nd isotope data of the granulite enclaves and the host granites in the DSGB to model the possible source components.

Available Sr–Nd isotope data show that the S-type granites in the DSGB spanned an $^{87}Sr/^{86}Sr(i)$ range from 0.720 to 0.730, an $\varepsilon_{Nd}(t)$ from −13.1 to −9.3, and an $\varepsilon_{Hf}(t)$ range from −14.6 to −6.5 (Fig. 13; Deng, 2003; Deng et al., 2004; Chen et al., 2011; Hsieh et al., 2008; Qi et al., 2007). Compared to the granulite enclaves, the S-type granites show less variation in $^{87}Sr/^{86}Sr(i)$ and similar $\varepsilon_{Nd}(t)$ and $\varepsilon_{Hf}(t)$ (Zhao et al., 2010; this study). As discussed above, the granulite enclaves can be divided into high-$^{87}Sr/^{86}Sr(i)$ and low-$^{87}Sr/^{86}Sr(i)$ groups. Here we use these two groups as two end-member components to model the melting source for the DSGB granites. The melting source for the granites contained 10–40% low-$^{87}Sr/^{86}Sr(i)$, and 60–90% high-$^{87}Sr/^{86}Sr(i)$ granulites (Fig. 13). Accordingly, it is reasonable to conclude that the granulite enclaves were the restites of the protoliths for the granites.

6.3. Genetic relationship between the granulite enclaves and host granites

As mentioned above, the granulite enclaves and the host granites are coherent in origin. Here we will discuss the genetic relationship between the granulite-facies metamorphism and the crustal anatexis in the region.

6.3.1. Ages of the granulite-facies metamorphism and granitic magmatism

Results of available zircon U–Pb dating and monazite electron microprobe (EMP) dating indicate that the metamorphic age of the granulites occurred during 260–250 Ma (Chen et al., 2011; Peng, 2006; Zhao et al., 2010). This age is consistent with the UHT metamorphism reported from the Kontum massif in the Indochina block (Nakano et al., 2004, 2007, 2009; Nam et al., 2001; Osanai et al., 2001, 2004; Owada et al., 2006, 2007). For instance, electron microprobe (EMP) dating of monazite showed that the timing of the metamorphism was ca. 260 Ma (Owada et al., 2006, 2007), and SHRIMP U–Pb zircon dating yielded a time of ca. 254 (Nam et al., 2001).

The granitic magmatism in this area is younger than the granulite-facies metamorphism. The majority of the available zircon U–Pb and monazite U–Th–Pb dating results revealed that the peraluminous granites were mainly formed at 240–230 Ma (Chen et al., 2011; Deng, 2003; Deng et al., 2004; Zhao et al., 2010). Such a time interval between the granulite-facies metamorphism and granitic magmatism reflects that the main stage of crustal anatexis postdated the peak metamorphism.

6.3.2. P–T comparison between the granulite-facies metamorphism and granitic magmatism

As discussed above, the granulite enclaves experienced three stages of metamorphism with the peak-metamorphic *P–T* condition of 950–1000 °C and 7.5–8.0 kbar. The *P–T* conditions were favorable for crustal anatexis, especially for fertile upper crustal rocks such as the protoliths of the granulite enclaves. This crustal remelting event was recorded in a few zircons, and in particular in the core–mantle portion of zircons in the Darongshan granite (Chen et al., 2011).

The previous magma temperature estimates for the granites in the SDGB show a large variation from 780 °C to 1000 °C (Charoy and Barbey, 2008; Chen et al., 2011; Fang, 1989). Based on the mineral assemblages of the granites, Charoy and Barbey (2008) considered that the granitic magmas of the Darongshan granitic complex were formed by biotite dehydration-melting with a pressure of 4.0–6.0 kbar and a temperature of 800–950 °C. Using a Zr saturation

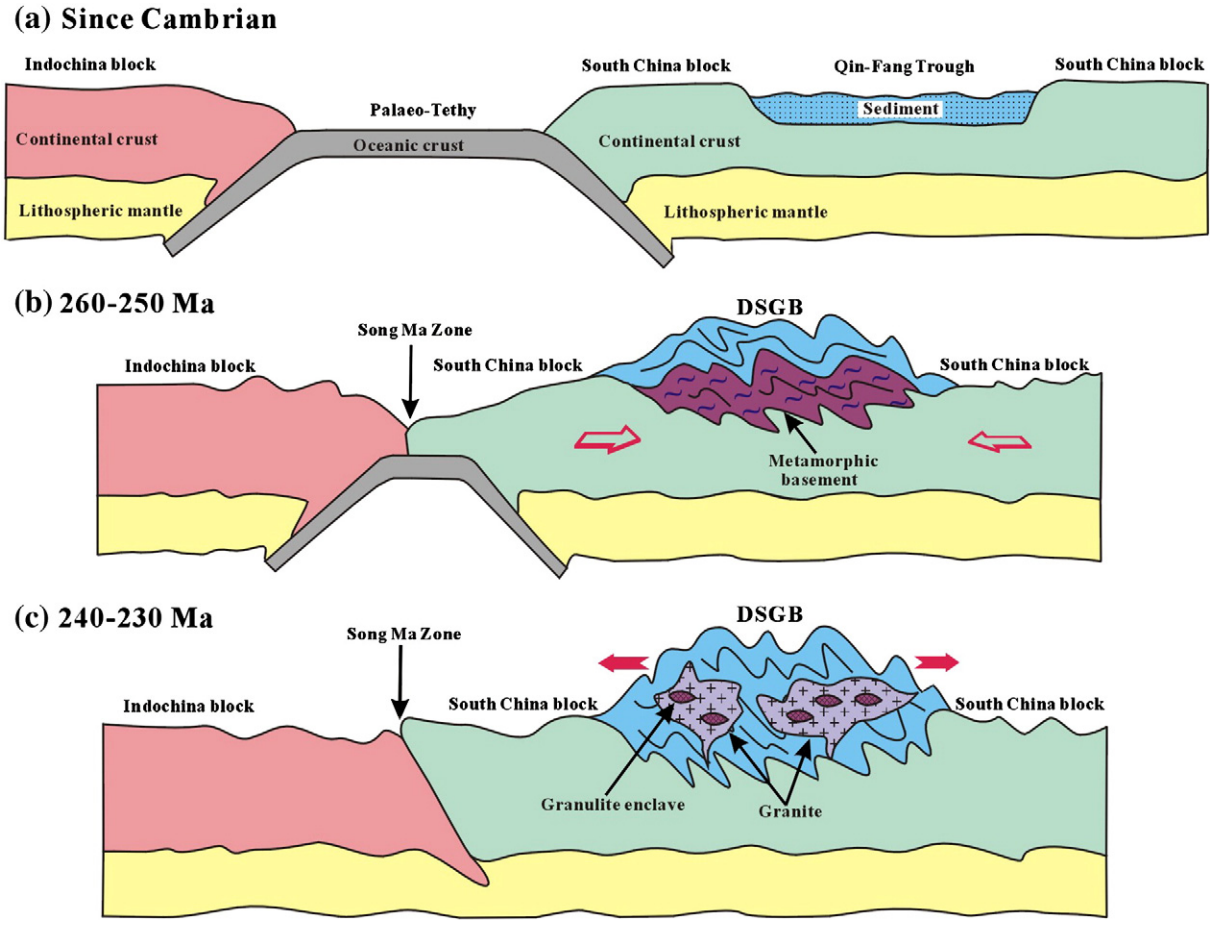

Fig. 15. A schematic cartoon showing the possible crustal evolution of the DSGB from early Paleozoic to early Mesozoic. See details in the text.

method of whole-rock geochemistry (Miller et al., 2003; Watson and Harrison, 1983, 2005), the temperature for the granites from the DSGB was calculated as 800–900 °C. In accordance with the dehydration-melting reaction of biotite (Fig. 9) and the experimental data from metapelite melting (Nair and Chacko, 2002; Patiño Douce and Beard, 1995; Viezeuf and Montel, 1994), the temperature for granitic magma melting should exceed 820 °C. Therefore, we selected $P = 4.0–6.0$ kbar and $T = 850–950$ °C to roughly represent the melting conditions for the granites.

The estimated melting *P–T* conditions for the granites plot along the retrograde metamorphic path (Fig. 9). Combining the timing of the peak metamorphism and granitic magmatism, we propose that the generation of the granitic magma mainly occurred during the exhumation and uplifting of the granulites. Similar cases have been recognized in the metasedimentary rocks and their host granites from the Tatra mountains of the western Carpathians (Janák et al., 1999), the Kontum massif in central Vietnam (Owada et al., 2007), and the Moldanubian unit of the Bohemian Massif (Žák et al., 2011).

6.3.3. The possible role of fluid in dehydration melting of the crustal protoliths

It is well known that water is crucial for granitic magma generation. The reason why the granitic magmatism mainly took place during the exhumation and uplifting of the granulites might be related to fluid. In accordance with the prograde reactions (1) and (2) that denoted fluid-absent dehydration melting of the metasedimentary protoliths, fluid was possibly lacking in the metamorphic system during the prograde metamorphic stage of the granulite enclaves. Also, some biotites were extremely rich in TiO_2 (up to 6.7%), and experienced HT metamorphism (>950 °C). This means that these boitites were stable during the peak metamorphism and that there was scarce fluid related to biotite decomposition. By contrast, biotite decomposition was widespread in the retrograde metamorphism, e.g., breakdown of biotite formed the second generation of orthopyroxene and fluid (Fig. 2h).

On the other hand, the SDGB experienced extensive thermal perturbation from the Permian Emeishan plume activity (ca. 260 Ma, e.g., Guo et al., 2004; Xu et al., 2001a, 2001b; Zhou et al., 2002), which possibly caused the dehydration of the metasedimentary protoliths before crustal thickening. This is consistent with the lack of muscovite and chlorite in the granulite enclaves. Another possible reason was the great depth of the metapelites (ca. 21–25 km, BGMRGX, 1985), which caused dehydration of clay minerals prior to crustal thickening.

The combined comparison of zircon and monazite U–Pb geochronology, *P–T* conditions between the granulite enclaves and the host granites, and the inferred fluid content variation trend through the metamorphic history, suggested that dehydration melting of the metasedimentary protoliths could be limited during the prograde and peak metamorphic stages. Instead, large-scale crustal anatexis may have occurred during the uplifting of the middle-lower crust.

6.4. Implications for regional crustal evolution

In summary, it is reasonable to conclude that the granulite enclaves in the DSGB were: (1) restites of the peraluminous granites; and (2) experienced a clockwise *P–T* path that was probably related to the Indo-Sinian collision between the SCB and Indochina block,

and Emeishan plume activity during the end of the Permian to the Triassic (Chen et al., 2011; Peng, 2006; Zhao et al., 2010, 2011). In the following section, we address the possible crustal evolution in the region by integrating the available geochronological and petrogenetic data with the regional geology (Fig. 15).

(1) Since Cambrian era (Fig. 15a). The SCB and the Indochina block were separated by the Paleo-Tethys Ocean. Previous studies on U–Pb ages of detrital zircons showed that the youngest inherited zircon in the granulite enclaves was ~564 Ma (Zhao et al., 2010), indicating that the protoliths have been deposited since Cambrian. According to the regional geology (BGMRGX, 1985), the Qin-Fang Trough deposited voluminous eroded materials from Cambrian to Permian with a total thickness of 21–25 km.

(2) 260–250 Ma (Fig. 15b). The closure of the eastern Paleo-Tethys Ocean led to the collision between the SCB and the Indochina block along the Song Ma suturing zone, and also the closure of the Qin-Fang Trough along the DSGB that had led to crustal thickening. This event exerted a strong effect on both of the SCB and the Indochina block (Chen et al., 2011; Lepvrier et al., 2008; Trung et al., 2006). In the Indochina block, the Kontum massif in central Vietnam experienced ultrahigh-temperature metamorphism in the late Permian (Nakano et al., 2004, 2007, 2009; Nam et al., 2001; Osanai et al., 2001, 2004; Owada et al., 2006, 2007). As a counterpart of the Kontum massif in the SCB (Chen et al., 2011), contemporaneous HT granulite-facies metamorphism occurred in the DSGB. Despite the difference of the high-grade metamorphism between the two blocks, both the UHT and HT granulites required rather high geothermal gradients (e.g., >30 °C/km) in the late Permian. This is probably a consequence of the thermal impact caused by the Emeishan plume (Chen et al., 2011; Owada et al., 2007; Peng, 2006; Zhao et al., 2010, 2011).

(3) 240–230 Ma (Fig. 15c). During the early Mesozoic (240–230 Ma), the thickened crust of the DSGB was subjected to post-collisional extension, which led to rapid uplifting of the high-grade metamorphic batholiths. During exhumation and unroofing of the lower-middle crust, large scale dehydration melting occurred to form the widely distributed peraluminous granites in the region.

7. Conclusions

On the basis of detailed mineralogical and geochemical studies of the granulite enclaves in the Indo-Sinian S-type granites from the DSGB in South China, the following conclusions can be made:

(1) The granulite enclaves in the DSGB experienced a three-stage metamorphism with a clockwise *P–T* path, genetically related to the collision between the South China and Indochina blocks, and the possible impact of the Emeishan plume activity. The sedimentary protoliths proceeded through the stability field of sillimanite, the assemblage of spinel + quartz at the peak-metamorphic stage, and the formation of Opx + Pl and Opx + Crd symplectites during the retrograde stage.

(2) The granulite enclaves and the host granites show linear correlations in major oxides and trace elements. They also show similar chondrite-normalized REE patterns, trace element spidergrams, and Sr–Nd isotopic compositions. All of these factors indicate a cogenetic origin: the granites were derived from partial melting of the metasedimentary rocks, and the granulite enclaves were restites of the source rocks.

(3) The combined mineralogical observations, *P–T* path, and geochemical results of the granulite enclaves, and their genetic relationship with the host granites, suggest that dehydration melting of the metasedimentary protoliths could have been limited during the prograde metamorphic stage. Instead, large scale crustal melting may have occurred during the stage of exhumation and uplifting of the lower-middle crust, forming the widespread peraluminous granites in the region.

Acknowledgments

This study was financially supported by the Chinese Academy of Sciences (KZCX2-YW-Q08-3-7 and KZCX1-YW-15-2). We sincerely thank L.L. Chen for electron microprobe analyses, and Y. Liu, G.Q. Hu, J.L. Ma, X.L. Tu and X.R. Liang for major and trace element and Sr–Nd isotope analyses. Valuable discussions with Profs. L.X. Tong, C.M. Wu, C.J. Wei, J.H. Guo and L.D. Ren are greatly appreciated. This paper has benefited from constructive comments and suggestions provided by Drs. C.H. Chen and W. Yang.

Appendix A. Supplementary data

Supplementary data to this article can be found online at doi:10.1016/j.lithos.2012.02.015.

References

Anderson, J.A.C., Price, R.C., Fleming, P.D., 1998. Structural analysis of metasedimentary enclaves: implications for tectonic evolution and granite petrogenesis in the southern Lachlan Fold Belt, Australia. Geology 26, 119–122.
Antunes, I.M.H.R., Neiva, A.M.R., Silva, M.M.V.G., Corfu, F., 2009. The genesis of I- and S-type granitoid rocks of the Early Ordovician Oledo pluton Central Iberian Zone (central Portugal). Lithos 111, 168–185.
Bertrand, P., Ellis, D.J., Green, D.H., 1991. The stability of sapphirine–quartz and hypersthene –sillimanite–quartz assemblages: an experimental investigation in the system FeO–MgO–Al_2O_3–SiO_2 under H_2O and CO_2 conditions. Contributions to Mineralogy and Petrology 108, 55–71.
Bhattacharya, A., Krishnakumar, K.R., Raith, M., Sen, S.K., 1991. An improved set of a-*X* parameters for Fe–Mg–Ca garnet and refinements of the orthopyroxene–garnet thermometer and the orthopyroxene–garnet–plagioclase–quartz barometer. Journal of Petrology 32, 629–656.
Brandt, S., Klemd, R., Okrusch, M., 2003. Ultrahigh-temperature metamorphism and multistage evolution of garnet–orthopyroxene granulite from the Proterozoic Epupa Complex, NW Namibia. Journal of Petrology 44, 1121–1144.
Bureau of Geology Mineral Resource of Guangxi Zhuang Autonomous Region (BGMRGX)., 1985. Reginal Geology of Guangxi Zhuang Autonomous Region. Geological Publishing House, Beijing, pp. 1–853 (in Chinese).
Carrington, D.P., Harley, S.L., 1995. Partial melting and phase relations in high-grade metapelites: an experimental petrogenetic grid in the KFMASH system. Contributions to Mineralogy and Petrology 120, 270–291.
Chappell, B.W., White, A.J.R., Wyborn, D., 1987. The importance of residual source material (restite) in granite petrogenesis. Journal of Petrology 28, 1111–1138.
Charoy, B., Barbey, P., 2008. Ferromagnesian silicate association in S-type granites: the Darongshan granitic complex (Guangxi, South China). Bulletin Geological Society of France 179, 13–27.
Chen, Y.D., Price, R.C., White, A.J.R., Chappell, B.W., 1989. Inclusions in three S-type granites from southeastern Australia. Journal of Petrology 30, 1181–1218.
Chen, Y.D., Price, R.C., White, A.J.R., Chappell, B.W., 1990. Mafic inclusion from the Glenbog and Blue Gum granite suites, southeastern Australia. Journal of Geophysical Research 95, 17757–17785.
Chen, T.Y., Sun, G.Y., Yao, Y.P., Chen, H., 1995. Peraluminous granites of East Tethys and their implication in Gondwana dispersion and Asian accretion. Journal of Asian Earth Sciences 18, 243–251.
Chen, C.H., Hsieh, P.S., Lee, C.Y., Zhou, H.W., 2011. Two episodes of the Indosinian thermal event on the South China Block: constraints from LA-ICPMS U–Pb zircon and electron microprobe monazite ages of the Darongshan S-type granitic suite. Gondwana Research 19, 1008–1023.
Clemens, J.D., Wall, V.J., 1988. Controls on the mineralogy of S-type volcanic and plutonic rocks. Lithos 21, 53–66.
Collins, W.J., 1996. Lachlan Fold Belt granitoids: products of three-component mixing. Transaction Royal Society of Edinburgh: Earth Science 87, 171–181.
Deer, W.A., Howie, R.A., Zussman, J., 1992. An Introduction to the Rock-forming Mineral, 2nd ed. Longman Group UK, Harlow. 232.
Deng, X.G., 2003. SHRIMP U–Pb zircon geochronological, geochemical and Sr–Nd isotopic study on the S-type granulites, southeastern Guangxi, China. Postdoctor Research Report. Guangzhou Institute of Geochemistry, Chinese Academy of Science, Guangzhou. (in Chinese with English abstract).
Deng, X.G., Chen, Z.G., Li, X.H., Liu, D.Y., 2004. SHRIMP U–Pb zircon dating of the Darongshan–Shiwandashan granitoid belt in Southeastern Guangxi. China. Geological Review 50, 426–432 (in Chinese with English abstract).
Didier, J., Barbarin, B., 1991. Enlcaves and Granite Petrology, Developments in Petrology. Elsevier, Amsterdam.
Du, Y.S., Collerson, K.D., Zhao, J.X., Pang, B.C., 1999. Characteristics and petrogenesis of granulite enclaves in S-type granites in the junction of Guangdong and Guangxi provinces. Acta Petrologica Sinica 15, 309–314 (in Chinese with English abstract).

Elburg, M.A., Nicholls, I.A., 1995. Origin of microgranitoid enclaves in the S-type Wilson's Promontory Batholith, Victoria: evidence for magma mingling. Australian Journal of Earth Sciences 42, 423–435.
Fang, Q.H., 1989. The plate-tectonic environment and genetic mechanism of the hypersthene granite at Darongshan, Guangxi. Journal of Southeast Asian Earth Sciences 3, 271–279.
Fitzsimons, I.C.W., Harley, S.L., 1994. The influence of retrograde cation exchange on granulite *P–T* estimates and a convergence technique for the recovery of peak metamorphic conditions. Journal of Petrology 35, 543–576.
Frost, B.R., Chacko, T., 1989. The granulite uncertainty principle: limitation on thermobarometry in granulites. Journal of Geology 97, 435–450.
Gomes, M.E.P., 2008. Geochemistry of microgranular enclaves and host granite from Telões (Vila Pouca de Aguiar), Northern Portugal. Chemie der Erde Geochemistry 68, 69–80.
Guo, F., Fan, W.M., Wang, Y.J., Li, C.W., 2004. When did the Emeishan mantle plume activity start? Geochronological and geochemical evidence from ultramafic-mafic dikes in southwestern China. International Geology Review 46, 226–234.
Harley, S.L., 1989. The origins of granulites: a metamorphic perspective. Geological Magazine 126, 215–247.
Harley, S.L., 1998. On the occurrence and characterization of ultrahigh-temperature (UHT) crustal metamorphism. In: Treloar, P.J., O'Brien, P. (Eds.), What Drives Metamorphism and Metamorphic Recations? : Geological Society, London, Special Publications, 138, pp. 81–107.
Hensen, B.J., 1987. *P–T* grids for silica-undersaturated granulites in the system MAS (n + 4) and FMAS (n + 3): tools for the derivation of *P–T* paths of metamorphism. Journal of Metamorphic Geology 5, 255–271.
Hensen, B.J., Harley, S.L., 1990. Graphical analysis of *P–T–X* relations in granulite facies metapelites. In: Brown, M., Ashworth, J.R. (Eds.), High-grade Metamorphism and Crustal Anatexis. Allen and Unwin, London, pp. 19–55.
Holdaway, M.J., Lee, S.M., 1977. Fe–Mg cordierite stability in high-grade pelitic rocks based on experimental, theoretical, and natural observations. Contributions to Mineralogy and Petrology 63, 175–198.
Hsieh, P.S., Chen, C.H., Yang, H.J., Lee, C.Y., 2008. Petrogenesis of the Nanling Mountains granites from South China: constraints from systematic apatite geochemistry and whole-rock geochemical and Sr–Nd isotope compositions. Journal of Asian Earth Science 33, 428–451.
Janák, J., Hurai, V., Ludhová, L., Thomas, R., 1999. Partial melting and retrogession during exhumation of high-grade metapelites, the Tatra mountains, western Carpathians. Physics and Chemistry of the Earth, Part A: Solid Earth and Geodesy 24, 289–294.
King, P.L., White, A.J.L., Chappell, B.W., Allen, C.M., 1997. Characterization and origin of aluminous A-type granites from the Lachlan Fold Belt, southeastern Australia. Journal of Petrology 38, 371–391.
Lepvrier, C., Maluski, H., 2008. The Triassic Indosinian Orogeny in East Asia. Comptes Rendus Geosciences 340, 75–82.
Lepvrier, C., Vuong, N.V., Maluski, H., Thi, P.T., Vu, T.V., 2008. Indosinian tectonics in Vietnam. Comptes Rendus Geosciences 340, 94–111.
Li, X.Q., Liu, W.J., Zhen, R.C., 1994. Formation of Qinzhou–Fangcheng folding belt and its geological influence. Guangxi Geology 7, 15–25 (in Chinese with English abstract).
Li, X.H., Li, Z.X., Zhou, H., Liu, Y., Kinny, P.D., 2002a. U–Pb zircon geochronology, geochemistry and Nd isotopic study of Neoproterozoic bimodal volcanic rocks in the Kangdian Rift of South China: implications for the initial rifting of Rodinia. Precambrian Research 113, 135–154.
Li, Z.X., Li, X.H., Zhou, H., Kinny, P.D., 2002b. Grenville-aged continental collision in South China: new SHRIMP U–Pb zircon results and implications for Rodinia configuration. Geology 30, 163–166.
Li, X.H., Li, Z.X., Sinclair, J.A., Li, W.X., Carter, G., 2006. Revisiting the "Yanbian Terrane": implications for Neoproterozoic tectonic evolution of the western Yangtze Block, South China. Precambrian Research 151, 14–30.
Li, X.H., Li, W.X., Li, Z.X., Liu, Y., 2008. 850–790 Ma bimodal volcanic and intrusive rocks in northern Zhejiang, South China: a major episode of continental rift magmatism during the breakup of Rodinia. Lithos 102, 341–357.
Li, X.H., Li, W.X., Li, Z.X., Lo, C.H., Wang, J., Ye, M.F., Yang, Y.H., 2009. Amalgamation between the Yangtze and Cathaysia Blocks in South China: constraints from SHRIMP U–Pb zircon ages, geochemistry and Nd–Hf isotopes of the Shuangxiwu volcanic rocks. Precambrian Research 174, 117–128.
Liang, X.Q., Li, X.H., 2005. Late Permian to Middle Triassic sedimentary records in Shiwandashan Basin: implication for the Indosinian Yunkai Orogenic Belt, south China. Sedimentary Geology 177, 297–320.
Liang, X.Q., Li, X.H., Qiu, Y.X., 2004. Intracontinental collisional orogeny during Late Permian–Middle Triassic in south China: sedimentary records of the Shiwandashan Basin. Acta Geologica Sinica 78, 301–307.
Liu, Y., Liu, H.C., Li, X.H., 1996. Simultaneous and precise determination of 40 trace elements in rock samples using ICP-MS. Geochimica 25, 552–558 (in Chinese with English abstract).
Lovering, J.F., White, A.J.R., 1969. Granulite and eclogitic inclusions from basis pipes at Delegate, Australia. Contributions to Mineralogy and Petro1ogy 21, 9–52.
Ma, L.F., 2002. Geological Atlas of China. Geological Publishing House, Beijing, pp. 1–348 (in Chinese).
Mass, R., Nicholls, I.A., Legg, C., 1997. Igneous and metamorphic enclaves in the S-type DEddick Granodiorite, Lachlan Fold Belt, SE Australia: petrographic, geochemical and Nd–Sr isotopic evidence for crustal melting and magma mixing. Journal of Petrology 38, 815–841.
McCulloch, M.T., Chappell, B.W., 1982. Nd isotope characteristics of S- and I-type granites. Earth and Planetary Science Letters 58, 51–64.
Meng, Q.R., Zhang, G.W., 1999. Timing of collision of the North and South China blocks: controversy and reconciliation. Geology 27, 123–126.
Miller, C.F., McDowell, S.M., Mapes, R.W., 2003. Hot and cold granites? Implication of zircon saturation temperatures and preservation of inheritance. Geology 31, 529–532.
Nair, R., Chacko, T., 2002. Fluid-absent melting of high-grade semipelites: P–T constraints on orthopyroxene formation and implications for granulite genesis. Journal of Petrology 43, 2121–2142.
Nakano, N., Osanai, Y., Owada, M., Nam, T.N., Tsunogae, T., Toyoshima, T., Binh, P., 2004. Decompression process of mafic granulite from eclogite to granulite facies under ultrahigh-temperature condition in the Kontum massif, central Vietnam. Journal of Mineralogical and Petrological Sciences 99, 242–256.
Nakano, N., Osanai, Y., Owada, M., Nam, T.N., Toyoshima, T., Binh, P., Tsunogae, T., Kagami, H., 2007. Geologic and metamorphic evolution of the basement complex in the Kontum massif, central Vietnam. Gondwana Research 12, 438–453.
Nakano, N., Osanai, Y., Owada, M., Hayasaka, Y., Nam, T.N., 2009. Permo-Triassic Barrovian-type metamorphism in the ultrahigh-temperature Kontum massif, central Vietnam: constraints on continental collision tectonics in Southeast Asia. Island Arc 18, 126–143.
Nam, T.N., Sano, Y.I., Terada, K., Toriumi, M., Ouynh, P.V., Dung, L.T., 2001. First SHRIMP U–Pb zircon dating of granulites from the Kontum massif (Vietnam) and tectonothermal implications. Journal of Asian Earth Sciences 19, 77–84.
Osanai, Y., Owada, M., Tsunogae, T., Toyoshima, T., Hokada, T., Long, T.V., Sajeev, K., Nakano, N., 2001. Ultrahigh-temperature politic granulites from Kontum massif, central Vietnam: evidence for East Asian juxtaposition at ca. 250 Ma. Gondwana Research 4, 720–723.
Osanai, Y., Nakano, N., Owada, M., Nam, T.N., Toyoshima, T., Tsunogae, T., Binh, P., 2004. Permo-Triassic ultrahigh-temperature metamorphism in the Kontum massif, central Vietnam. Journal of Mineralogical and Petrological Sciences 99, 225–241.
Owada, M., Osanai, Y., Hokada, T., Nakano, N., 2006. Timing of metamorphism and formation of garnet granite in the Kontum massif, central Vietnam: evidence from monazite EMP dating. Journal of Mineralogical and Petrological Sciences 101, 324–328.
Owada, M., Osanai, Y., Nakano, N., Matsushita, T., Nam, T.N., Tsunogae, T., Toyoshima, T., Binh, P., Kagami, H., 2007. Crustal anatexis and formation of two types of granitic magmas in the Kontum massif, central Vietnam: implications for magma processes in collision zones. Gondwana Research 12, 428–437.
Pang, B.C., 2001. The types, features and genesis of enclaves in granitoids in the junction of Guangdong and Guangxi. Journal of Mineralogy and Petrology 21, 8–13 (in Chinese with English abstract).
Patiño Douce, A.E., 1993. Titanium substitution in biotite: an empirical model with applications to thermometry, O_2 and H_2O barometries, and consequences for biotite stability. Chemical Geology 108, 133–162.
Patiño Douce, A.E., Beard, J.A., 1995. Dehydration-melting of biotite gneiss and quartz amphibolite from 3 to 15 kbar. Journal of Petrology 36, 707–738.
Patiño Douce, A.E., Johnston, A.D., Rice, J.M., 1993. Octahedral excess mixing properties in biotite: a working model with applications to geobarometry and geothermometry. American Mineralogist 78, 113–131.
Peng, S.B., 2006. Discovery and significance of the ultrahigh temperature granulite enclaves from Shiwandashan granites in southeast Guangxi Province, China. Abstract volume of 2006 Petrology and Earth Dynamics in China. Nanjing University, Nanjing, pp. 402–403 (in Chinese).
Peng, S.B., Fu, J.M., Liu, Y.H., 2004. The discovery and significance of A-type charnockite in southeast Guangxi province, China. Science Technology and Engineering 4, 832–834 (in Chinese with English abstract).
Qi, C.S., Deng, X.G., Li, W.X., Li, X.H., Yang, Y.H., Xie, L.W., 2007. Origin of the Darongshan–Shiwandashan S-type granitoid belt from southeastern Guangxi: geochemical and Sr–Nd–Hf isotopic constraints. Acta Petrologica Sinica 23, 403–412 (in Chinese with English abstract).
Qiu, Y.X., Liang, X.Q., 2006. Evolution of basin-range coupling in the Yunkai Dashan-Shiwan Dashan area, Guangdong and Guangxi: with a discussion of several tectonic problems of South China. Geological Bulletin of China 25, 341–347 (in Chinese with English abstract).
Raith, M., Karmakar, S., Brown, M., 1997. Ultra-high-temperature metamorphism and multi-stage decompressional evolution of sapphirine granulite from the Palni hill ranges, southern India. Journal of Metamorphic Geology 15, 379–399.
Ring, U., Brandon, M.K., Willett, S.D., Lister, G.S., 1999. Exhumation processes. Geological Society, London, Special Publications 154, 1–27.
Rudnick, R.L., Gao, S., 2003. Composition of the continental crust. In: Rudnick, R.L. (Ed.), The Crust. Treatise on Geochemistry, Vol. 3. Elsevier, Amsterdam, pp. 1–64.
Sajeev, K., Osanai, Y., 2004. Osumilite and spinel + quartz from Sri Lanka: Implication for UHT conditions and retrograde P–T path. Journal of Mineralogical and Petrological Sciences 99, 320–327.
Sajeev, K., Osanai, Y., Santosh, M., 2004. Ultrahigh-temperature metamorphism followed by two-stage decompression of garnet–orthopyroxene–sillimanite granulites from Ganguvarpatti, Madurai block, southern India. Contributions to Mineralogy and Petrology 148, 29–46.
Santosh, M., Tsunogae, T., Li, J.H., Liu, S.J., 2007. Discovery of sapphirine-bearing Mg–Al granulites in the North China Craton: implication for Paleoprotezoic ultrahigh temperature metamorphism. Gondwana Research 11, 263–285.
Sengupta, P., Sen, J., Dasgupta, S., Raith, M., Bhui, U.K., Ehl, 1999. Ultra-high temperature metamorphism of metapelitic granulite from Kondapalle, Eastern Ghats Belt: Implications for the Indo-Antarctic correlation. Journal of Petrology 40, 1065–1087.
Shaw, D.M., 1972. The origin of the Apsley gneiss. Canadian Journal of Earth Science 9, 18–35.
Silva, M.M.V.G., Neiva, A.M.R., Whitehouse, M.J., 2000. Geochemistry of enclaves and host granites from the Nelas area, central Portugal. Lithos 50, 153–170.
Sun, S.S., McDonough, W.F., 1989. Chemical and isotopic systematics of oceanic basalts: implication for mantle composition and process. In: Saunder, A.D., Norry, M.J.

(Eds.), Magmatism in the ocean basins: Geological Society, London Special Publications, 42, pp. 313–345.
Trung, N.M., Tsujimori, T., Itaya, T., 2006. Honvang serpentinite body of the Song Ma fault zone, Northern Vietnam: a remnant of oceanic lithosphere within the Indochina-South China suture. Gondwana Research 9, 225–230.
Vielzeuf, D., Montel, J.M., 1994. Partial melting of metagreywackes. Part I: fluid-absent experiments and phase relationships. Contributions to Mineralogy and Petrology 117, 375–393.
Waight, T.E., Maas, R., Nicholls, I.A., 2001. Geochemical investigations of microgranitoid enclaves in the S-type Cowra Granodiorite, Lachlan Fold Belt, SE Australia. Lithos 56, 165–186.
Wall, V.J., Clemens, J.D., Clarke, D.B., 1987. Models for granitiod evolution and source compositions. Journal of Geology 95, 731–749.
Wang, S.N., 1987. A preliminary study on inclusions in crust-derived granites from Darongshan–Shiwandashan belt. Geology of Guangxi 6, 29–38 (in Chinese with English abstract).
Wang, Y.J., Fan, W.M., Cawood, P.A., Ji, S.C., Peng, T.P., Chen, X.Y., 2007. Indosinian high-strain deformation for the Yunkaidashan tectonic belt, south China: Kinematics and $^{40}Ar/^{39}Ar$ geochronological constraints. Tectonics 26, TC6008. doi:10.1029/2007TC002099.
Watson, E.B., Harrison, T.M., 1983. Zircon saturation revisited: temperature and composition effect in a variety of crustal magmas types. Earth and Planetary Science Letters 64 (2), 295–304.
Watson, E.B., Harrison, T.M., 2005. Zircon thermometer reveals minimum melting conditions of earliest earth. Science 308, 841–844.
White, A.J.R., Chappell, B.W., 1977. Ulrtametamorphism and granitoids genesis. Tectonophysics 43, 7–22.
Williamson, B.J., Downes, H., Thirlwall, M.F., Beard, A., 1997. Ceochemical constraints on restite composition and unmixing in the Velay anatectic granite, French Massif Central. Lithos 40, 295–319.
Winker, H.G.F., 1967. Petrogenesis of Metamorphic Rocks, 2nd Ed. Springer-Verlag, New York.
Xu, X.S., Yin, F.G., Wan, F., Liang, Z.H., Wei, B.D., Zhang, J.D., 2001a. The migration of the Qinzhou–Fangcheng trough in Guangxi and associated sedimentary–tectonic transform surfaces. Sedimentary Geology and Tethyan Geology 21, 1–10 (in Chinese with English abstract).
Xu, Y.G., Chung, S.L., Jahn, B.M., Wu, G.Y., 2001b. Petrological and geochemical constraints on the petrogenesis of Permian-Triassic Emeishan flood basalts in southwestern China. Lithos 58, 145–168.
Ye, M.F., Li, X.H., Li, W.X., Liu, Y., Li, Z.X., 2007. SHRIMP zircon U–Pb geochronological and whole-rock geochemical evidence for an early Neoproterozoic Sibaoan magmatic arc along the southeastern margin of the Yangtze Block. Gondwana Research 12, 144–156.
Yin, H.F., Wu, S.B., Du, Y.S., Peng, Y.Q., 1999. South China defined as part of Tethyan archipelagic ocean system. Earth Science-Journal of China University of Geosciences 21, 1–12 (in Chinese with English abstract).
Žák, J., Verner, K., Finger, F., Faryad, S.W., Chlupáčová, M., Veselovsk, F., 2011. The generation of volumious S-type granites in the Moldanubian unit, Bohemian Massif, by rapid isothermal exhumation of the metapelitic middle crust. Lithos 121, 25–40.
Zhao, L., Guo, F., Fan, W.M., Li, C.W., Qin, X.F., Li, H.X., 2010. Crustal evolution of the Shiwandashan area in South China: Zircon U–Pb–Hf isotopic records from granulite enclaves in Indo-Sinian granites. Chinese Science Bulletin 55 (19), 2028–2038.
Zhao, L., Guo, F., Fan, W.M., Li, C.W., Qin, X.F., Li, H.X., 2011. Late Paleozoic ultrahigh-temperature metamorphism in South China: a case study of granulite enclaves in the Shiwandashan granites. Acta Petrologica Sinica 27, 1707–1720 (in Chinese with English abstract).
Zhou, M.F., Malpas, J., Song, X.Y., Robinson, P.T., Sun, M., KennEdy, A.k., Lesher, C.M., Keays, R.P., 2002. A temporal link between the Emeishan large igneous province (SW China) and the end-Guadalupian mass extinction. Earth and Planetary Science Letters 196, 113–122.